WAVE-CURRENT-TURBULENCE INTERACTIONS IN A HIGH-FLOW TIDAL CHANNEL

by

Colleen Wilson

Submitted in partial fulfillment of the requirements
for the degree of Master of Science

at

Dalhousie University
Halifax, Nova Scotia
March 2018

© Copyright by Colleen Wilson, 2018

TABLE OF CONTENTS

LIST OF TABLES

LIST OF FIGURES

ABSTRACT

Grand Passage has been identified for in-stream tidal turbine development as a predictable, high power density, renewable energy source, and is the site for this work. A shore-connected bottom mounted Acoustic Doppler Current Profiler (ADCP) sampling at 2 Hz for 10 days in January/February 2015 spanning a storm with 80 km/h northerly winds recorded tidal current maximum speeds of approximately 2 m/s. Wave height and wave number are estimated from the velocity variance vertical structure in the gravity wave band. Independent estimates of the wavenumber are obtained from the measured phase speed, and compared to the predictions of linear wave theory, including the effects of vertical shear. The analysis also yields an estimate of the turbulence dissipation rate. Maximum wave heights were approximately 2 m, when current and waves oppose. During low wave conditions, the mid-depth turbulent dissipation rate was O(10^{-4}) W/kg, and increased with larger waves.

List of Abbreviations and Symbols Used

Roman symbol	Description	Units
a	wave amplitude	m
c	wave phase speed	m/s
f	observed frequency	Hz
g	acceleration due to gravity	m/s^2
h	water depth	m
H_s	significant wave height	m
k	wavenumber	m^{-1}
L	beam separation	m
r	radial distance from ADCP	m
t	time	s
u	across-channel velocity	m/s
U	across-channel mean flow	m/s
v	along-channel velocity	m/s
V	along-channel mean flow	m/s
V_0	along-channel mean mid-depth flow	m/s
$\tilde{V}$	V term from *Kirby and Chen* (1989)	m/s
w	vertical velocity	m/s
x	horizontal distance	m
z	vertical coordinate to mean water level	m

Greek symbol	Description	Units
ϵ	dissipation rate	W/kg
η	surface elevation	m
θ	ADCP beam angle	^{0}
λ	wavelength	m
σ_η	square root of surface elevation variance	m

Greek symbol	Description	Units
σ_D^2	Doppler noise	m^2/s^2
σ_p^2	pressure variance	m^2
σ_u^2	u velocity variance	m^2/s^2
σ_w^2	wave variance	m^2/s^2
σ_{1-4}^2	beam velocity variance	m^2/s^2
σ'^2	turbulent noise	m^2/s^2
τ	beam lag	s
ω	intrinsic angular frequency	Hz
ω_0	observed angular frequency	Hz

ACKNOWLEDGEMENTS

Thank you to supervisor Alex Hay, and committee members Tony Bowen, Richard Karsten and Greg Wilson for their guidance, members of the Hay lab for assistance throughout the completion of this thesis and friends, family, coaches and teammates for their support.

This project was supported by the EcoEnergy program of Natural Resources Canada, and by graduate fellowships from the Government of Nova Scotia and the Government of Ontario.

CHAPTER 1

INTRODUCTION

Tidal energy developers are concerned with the lack of knowledge regarding the variability of wave and tidal current conditions. The first in-stream test turbine in the Bay of Fundy, NS, installed in the Minas Basin in 2009, was destroyed within three weeks because of unexpectedly high tidal velocities. Clearly it is important to properly characterize the tidal flows before design and deployment of the turbines. This research examines interactions between waves and tidal currents in Grand Passage, NS. Storm events with high wind speeds are given particular attention as these have the potential to generate the highest waves - depending on the direction of the tide - and therefore the most significant effects.

1.1 Background

1.1.1 In-Stream Tidal Power

Harnessing tidal energy began with Roman mills, and until the 1990's focussed on barrages with high initial costs and environmental impacts. Tidal power generation research has turned to in-stream turbines as a predictable, high power density and minimal visual impact renewable energy source. A critical aspect of in-stream tidal power implementation is resource assessment: i.e. estimating the maximum extractable power, which depends on site-specific flow, topographic conditions and assumptions (*Blunden and Bahaj*, 2006). Canada has an estimated 191 potential sites for tidal energy generation with an estimated 42 GW of untapped energy, over 70% of Canada's current annual consumption (*Fisch*, 2016). Kinetic power varies as flow speed cubed, however *Garrett and Cummins* (2005) determined that there was no simple relationship between the maximum mean power for a channel connecting two large basins and the undisturbed kinetic energy flux. Tidal currents over 4 knots, or 2 m/s can be used for power extraction (*Bahaj et al.*, 2007). Many

extractable power estimates assume non-divergent tidal flow, which are independent of position along the channel, and require the channel to be small relative to the tidal wavelength (*Cummins*, 2011). However this assumption underestimates the available power, which may actually vary with position .

Various schemes to harness tidal energy have been proposed for tidal channels around the world. A site resource assessment conducted for East River in New York City found that the theoretical power density derived from measured current speeds was an order of magnitude higher than estimates from US national resource assessments, and was significantly influenced by the time averaging window, highlighting the importance for measurements at the turbine scale (*Gunawan et al*., 2014). Verdant Power installed an energy project in East River, NY, between 2006-2008 with six 70 MWh turbines. The site was licensed in January 2012 for a 1.05 MW array of 30 turbines (*VanZwieten et al*., 2014). In-stream power generation has also been investigated in the UK; in Northern Ireland twin 16 m diameter, 1.2 MW SeaGen turbines were deployed by Marine Current Turbines Ltd., the first turbines to be connected to a grid (*Ashall et al*., 2016); the European Marine Energy Centre (EMEC), a facility for open-sea, grid-connected wave and tide instrument testing in Orkney, has been used for turbine prototype tests including OpenHydro's 250 kW turbine in 2008, Andritz Hydro Hammerfest's 1MW turbine in 2011, Atlantis Resources Corporation's 1MW turbine which rotates at slack tide in 2011, French GDF Suez Voith Hydro turbine, and Alstrom's turbine in 2012 (*Zhou et al*., 2014).

In Canada, the Bay of Fundy, with flow speeds exceeding 5 m/s, and a water flux of 10^6 m^3/s is an obvious candidate for tidal power. In 2009, OpenHydro deployed a 10 m diameter turbine in Minas Passage which was destroyed, and a more robust 16 m diameter turbine in November 2016. The American side of the entrance to the Bay of Fundy has also been identified as a promising site for in-stream tidal development, with potential tidal power sites mostly located in passages linking smaller bays with the Bay of Fundy (*Brooks*, 2006). The turbine deployed in Cobscook Bay in 2012 was the first in-stream tidal energy system to deliver power to a US electricity grid (*VanZwieten et al*., 2014). According to the Energy Nova Scotia COMFIT Power Status in May 2016, three sites in the Digby area were approved for 0.5-1.95 MW tidal projects in 2011/2012, with anticipated in service dates of December 2018.

Kinetic power extraction reduces the flow of water through the region, and bulk kinetic energy calculations overestimate power because they do not account for this reduction. *Atwater and Lawrence* (2011) analytically determined a physical limit to extraction of 38% of the channel fluid power, which would result in a bulk flow reduction of 58%. In general engineering design however, extraction should not decrease the baseline scenario by more than 5-10%, far below the physical limit (*Polagye et al*., 2009). *Polagye et al*. (2009) used a 1D channel model with varying rows of in-stream tidal turbines represented as flow discontinuities, to determine the power dissipation changes and suggested it would be possible to produce 210 MW with a 5% decrease to the barotropic tidal regime in Puget Sound, Washington. *Ahmadian and Falconer* (2012) used a hydro-environmental model of three formations of 1000, 10 m diameter turbines to predict that turbine arrays in the Severn Estuary and Bristol Channel would cause immediate but localized water level changes, with negligible impact on maximum water level. They found that the tidal stream decreased up and down stream from the turbines, and accelerated at the sides and that a less dense array produced more power. *Cummins* (2013) investigated extracting power from a split channel, such as when an island divides a channel into two sections, and found the change in transport to be 50-71% in the impeded channel. *Yang et al*. (2014) used a FVCOM 3D model of Tacoma Narrows, Washington, to demonstrate that extracting tidal energy has a greater impact on the potentially more environmentally detrimental flushing time of a channel than reducing the volume flux, but that many turbines are needed before changes to the far field conditions occur.

For the Bay of Fundy, *Karsten et al*. (2008) predicted that a 2.5 GW extraction would reduce the flow by less than 5% and suggested that a maximum of 7 GW could be extracted from Minas Passage, but that extraction of this much energy would drive the Bay of Fundy - Gulf of Maine system closer to resonance, increasing the tidal range. Extracting maximum power would cause a flow reduction of over 30% in Minas Passage, a decrease in the tidal amplitude by >2m in the upper BoF, and an increase by a maximum of 0.25 m on the NE coast of USA. This agreed with previous estimates suggesting that adding a tidal barrage across Minas Passage would cause an increase in tidal amplitude by 20-30% along the coast of Maine and Massachusetts. In support, *Hasegawa et al*. (2011) used a 3D model to suggest that with maximum power extraction of 7.6 GW in Minas Passage, their model suggested a 40% decrease in M2 tidal current speed in the BoF, a decrease in the tidal

amplitude by 2.4 m in the upper BoF, and an increase by 0.2 m in Massachusetts Bay.

1.1.2 Previous Studies of Wave Current Interactions in Tidal Channels

For the purposes of this research, a tidal channel includes tidal rivers and estuaries, tidal inlets and channels between islands or headlands. Waves and currents exchange energy, so a linear superposition of the maximum wave scenario and maximum current scenario is not necessarily accurate when estimating turbine loading, as the maximum conditions could occur simultaneously. When waves propagate into an opposing current, wavelength decreases and wave heights increase, possibly to the point of breaking, whereas when following a current wave heights decrease (*Peregrine*, 1976). If the opposing current velocity approaches the wave group velocity, wave blocking may occur (*Ris and Holthuijsen*, 1997). Wave-current interactions can change the momentum balance either through enhanced bottom friction (*Grant and Madsen*, 1979, 1986) and (*Nielsen*, 1992) or through the wave radiation stresses (*Longuet-Higgins and Stewart*, 1964).

Hashemi et al. (2015) used three numerical models for the Irish Sea and found that including forces from radiation stresses caused a decrease in tidal power of 3% (average wave) and 7% (extreme wave), while including enhanced bottom friction caused a decrease of 2% and 6%. However, when the model included both radiation stresses and enhanced bottom friction, the decrease in tidal power was 15% and 20% respectively. Furthermore, they noted that wave forces had a greater effect on opposing currents. *Wolf and Prandle* (1999) studied the effects of water depth and barotropic tidal currents on surface waves, as well as the effects of waves on tidal currents and concluded that linear wave theory should be accurate for depths greater than 12.5 m and wave heights less than 5 m. In comparison, using the empirical ratio of maximum wave height at breaking to water depth outlined in *Mei* (1989) of 0.7-1.2, the significant wave height would range from approximately 8.4 m-14.3 m for linear wave theory to hold in 12.5 m of water. *Wolf and Prandle* found that reduced tidal current speed correlated with higher waves due to increased bottom friction. The tidal current was found to decrease in proportion to the magnitude and direction of the waves relative to the current, suggesting that the variation of high frequency waves was consistent with the current refraction. *Hashemi et al*. (2016) proposed an analytical model based on linear wave theory, with the assumption of deep water and a quasi-steady

state. They calculated a 60% increase in wave height when the current opposed the waves, and a 20% decrease when the waves followed the current. *Rusu et al*. (2011) modelled the Tagus estuary and also found that currents modified the shape of the wave spectrum, which in turn impacted the wave parameters, such as significant wave height and mean wave period.

Dodet et al. (2013) studied WCI in a wave-dominated tidal inlet on the west coast of Portugal and, based on *in situ* data and the hydrodynamical model SELFE coupled with SWAN, found that WCI had a significant impact on the hydrodynamics of the inlet. During the flood tide, incident waves were refracted by currents at the entrance of the inlet, which caused wave heights to increase by up to 10% on the main channel margins, and decrease by up to 10% along-channel. During the ebb tide, the opposing current increased wave steepness and whitecapping dissipation, and caused the significant wave height to increase locally by over 20%. Waves travelling in the channel quickly dissipated to less than 50% of the initial values, indicating a strong attenuation of wave height on the ebb tide. The current-induced modification of the wavefield had a "minor impact on the currents in the channel (less than 0.05 m/s [sign not stated]) but could reach up to 0.5 m/s at the entrance of the inlet where [there was] more energetic breaking".

There have been a few studies of WCI focussing on radiation stresses. *Dodet et al*. (2013) found that during the ebb, the radiation stresses are greater than during flood due to more intense wave breaking in shallower water and therefore, there is higher setup during ebb tide. *Wargula et al*. (2014) measured water level, currents and waves with an ADCP in a shallow tidal inlet and found the dominant terms in the momentum balance to be the along-inlet pressure gradient, bottom stress and wave radiation stress gradient. Near the inlet, the model simulations suggested that the cross shore radiation stress gradient due to wave dissipation drives flow into the inlet and increases water levels in the interior lagoon. Within the main inlet, the primary force balance is the pressure gradient and bottom stress with the wave radiation stress only significant in storm conditions. However, in shallower areas the wave radiation stress and pressure gradient were equal and both balance the bottom stress.

1.1.2.1 Numerical Modelling

WCI have implications for modelling wave heights and currents, yet have often been neglected due to the additional computational requirements. *Ardhuin et al*. (2012) reviewed the performance of numerical wave prediction models in the presence of strong currents and found that including currents reduces errors in wave height prediction by over 30%.

Simulating WAves Nearshore (SWAN) (*Booij et al*., 1997) is a model applicable to coastal areas where turbines would be deployed. *Rusu et al*. (2011) tested the performance of SWAN for the Tagus estuary in Portugal, with and without tide levels and currents, and found improved results for significant wave height, period and modulations when tidal effects are included, with the simulated ebb tide increasing wave heights by up to 60%, and the flood decreasing by up to 20%. *van der Westhuysen* (2012) used a SWAN hindcast model of the Wadden Sea, and found that wave heights were significantly overestimated due to not accounting for partial wave blocking in opposing currents. They presented a new form for the enhanced breaking dissipation of waves on an opposing current. *Saruwatari et al*. (2013) conducted SWAN simulations for various sites in the Orkneys, finding an increase in wave height by 150-200% on an opposing current, and that wave energy in the Pentland Firth changed by +/- 60% due to tidal effects. The three aforementioned studies demonstrated that SWAN overestimates the significant wave height in strong opposing currents.

1.1.3 Turbulence

Richardson (1922) described turbulent flow as being composed of eddies of different sizes, of which the larger are unstable and break into smaller. The energy is passed down through the eddies, until dissipated by the fluid viscosity. With respect to in-stream tidal energy, turbulence is an important factor with respect to fatigue and extreme loading on a turbine. *Mycek et al*. (2014a,b) examined the impact of ambient turbulence intensity on a 3-bladed horizontal axis turbine. They found an increase in performance fluctuations, which will cause increased fatigue on the turbine. Higher ambient turbulence intensity was however found to decrease wake, which increase power output when multiple turbines interact.

Measuring turbulence in the field in > 2 m/s flows is a significant challenge. *McMillan et al*. (2016) found that turbulent kinetic energy dissipation rates estimated from ADCP data agreed within a factor of 2 to estimates from shear probes in Grand Passage, with values from the ADCP being the higher. This difference was attributed to the 40 m lateral separation between the ADCP and shear probe moorings. In a subsequent paper, *McMillan and Hay* (2017) found that dissipation rates computed with spectral integral and structure function methods agreed to within 16%, which further supported the hypothesis of the factor of 2 difference being due to instrument separation and spatial variability of turbulence. The ADCP also agreed with the shear probe measured dissipation variation with flow speed and ebb-flood asymmetry. They concluded that ADCPs are able to make remote estimates of turbulence in high flow tidal regions. *McMillan et al*. examined only times at which there was no evidence of wind-wave motions at the depths of their measurements.

1.2 Thesis Objectives

The science questions pursued in this thesis are:

- What are the values, during storm conditions, of wave heights as a function of tidal phase?
- Are the resulting wave number and frequency estimates consistent with the predictions of linear wave theory?
- Do waves have a discernible effect on the vertical profile of Eulerian mean velocity in high flow conditions?
- Is the turbulence dissipation rate at mid-depth influenced by waves?

1.3 Importance and Timeliness

The questions posed in this thesis are important on both a basic scientific, as well as applied level. With respect to significance to basic science, the results of this thesis will contribute to an improved understanding of wave-current-turbulence interactions in high flow conditions,

and to new insights into the advantages and limitations of acoustic Doppler systems for remote measurement of waves, currents, and turbulence in high flow, high wave conditions.

The applications of this work pertain to the implementation of tidal turbines, specifically to improve knowledge of flow variability in tidal passages targeted for in-stream tidal energy development. The Bay of Fundy has been identified as the best potential site for tidal power generation in North America. It has been estimated that the power to supply 750,000 homes (about double the current Nova Scotia total) could be obtained by harnessing the tidal current in the Minas Basin alone without significantly influencing the peak tide height, and models indicate that there could be over seven times that potential over the whole Bay of Fundy (*Karsten et al*., 2013).

1.4 Thesis Organization

Chapter 2 summarizes the relevant aspects of linear wave theory, including wave propagation on a current both with and without vertical shear. The Kemp-Simons effect and Groeneweg-Klopman theory, are discussed. Chapter 2 also briefly summarizes the work by Lumley and Terray on turbulence spectrum distortion by waves. The field site, instrumentation and storm conditions are described in Chapter 3. The data processing section methods are explained in Chapter 4. The results are presented in Chapter 5. Finally, Chapter 6 summarizes the results and conclusions of this project in the context of past studies and theory.

CHAPTER 2

THEORY

2.1 Linear Wave Theory

The surface elevation of a wave, η, can be represented by

$$\eta = a\sin(kx - \omega t) \tag{2.1}$$

where a is the wave amplitude, k is the wavenumber (i.e. $2\pi/\lambda$, λ being the wavelength) and ω is the angular frequency. The horizontal and vertical velocity components given by linear theory in water of arbitrary depth are respectively given by (*Kundu and Cohen*, 2004),

$$u = a\omega\frac{\cosh k(z+h)}{\sinh kh}\sin(kx - \omega t) \tag{2.2}$$

$$w = a\omega\frac{\sinh k(z+h)}{\sinh kh}\cos(kx - \omega t) \tag{2.3}$$

and the pressure fluctuation

$$p' \equiv p + \rho g z \tag{2.4}$$

$$p' = \frac{\rho a\omega^2}{k}\frac{\cosh k(z+h)}{\sinh kh}\cos(kx - \omega t) \tag{2.5}$$

where h is the water depth, and z is the vertical coordinate relative to mean water level

with positive upward. The dispersion relationship ω for no ambient current is

$$\omega = \sqrt{gk \tanh kh}, \tag{2.6}$$

Deep water waves occur when $kh \gg 1$, and shallow water waves when $kh \ll 1$. Practically, waves are considered deep when $h > 0.28\lambda$, or $kh > 1.75$ (*Kundu and Cohen*, 2004). In deep water, particle orbits are circular and decay exponentially with depth. The pressure change due to presence of waves also decays exponentially, and waves are detectable by a pressure sensor mounted on the bottom only with wavelengths greater than approximately twice the water depth.

The significant wave height H_s can be calculated from the variance of the surface elevation or velocity time series measured in narrow-banded waves, i.e. such that the wave heights are Rayleigh-distributed, via the following relationships (*Thornton and Guza*, 1983)

$$H_s = 4\sigma_\eta \tag{2.7}$$

$$H_s = \frac{4\sigma_w}{\sqrt{gk \tanh kh}} \tag{2.8}$$

$$H_s = \frac{4\sigma_u \sqrt{\tanh kh}}{\sqrt{gk}} \tag{2.9}$$

where σ_η is the square-root of the surface elevation variance, and σ_w and σ_u are the square roots of the vertical and horizontal velocity variances at the surface, respectively.

The significant wave height from the pressure measurements is calculated with the pressure variance and k_P,

$$H_s = 4\sigma_p \cosh k_P h \tag{2.10}$$

where σ_p is calculated from the integration of the spectral peak in the waveband. The

$\cosh k_P h$ term accounts for the attenuation of pressure with depth.

2.2 Waves on a Uniform Current

The dispersion relation for waves on a uniform current is given by

$$\omega_0 = \omega + \mathbf{k} \cdot \mathbf{V} \tag{2.11}$$

where ω is the intrinsic frequency given by Equation 2.6, ω_0 is the observed frequency at a fixed point, **k** is the wave vector, and **U** is the horizontal mean flow velocity. Letting V be the mean flow speed, and α the angle between **k** and **V**, Equation 2.11 becomes

$$\omega_0 = \omega + Vk\cos\alpha \tag{2.12}$$

Thus, when waves and currents are perpendicular, the current has no effect on the waves. As discussed by *Mei et al*. (2005), for waves travelling with the current there are two possible scenarios: (a) either wavelength, intrinsic phase and group velocity increase or, (b) for magnitude of intrinsic phase and group velocity less than $U\cos\alpha$, wave crests and wave energy are swept along with current. For waves opposing a current, there are four possibilities: (1) both wave energy and crests move upstream; (2) wave energy moves downstream while crests move upstream; (3) energy held stationary in space while crests appear to move upstream; (4) no waves are possible (blocking). Figure 2.1 is similar to a plot in *Mei et al*. (2005), altered using values relevant to Grand Passage in storm conditions: i.e. 2 m/s current, 28 m water depth, and 7 s period waves. The figure demonstrates that only two of the cases outlined by *Mei et al*. (2005) are likely to occur: for waves with the current the wavelength, intrinsic phase and group velocity increase, and for waves against the current both wave energy and crests move upstream.

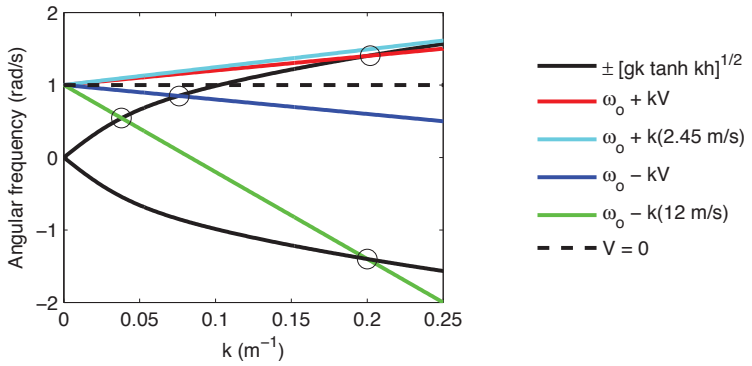

Figure 2.1: Demonstrates the expected values to occur for this experiment based on 7 s waves propagating with (blue) and against (red) a 2 m/s current in 28 m water depth. The intersection of the blue and solid black line show that for waves with the current and values of ω, ω_o, k and V representative of Grand Passage, scenario (a) occurs. The intersection of the red and black lines shows that for waves against the intrinsic curve and the observed angular frequency with the Doppler shift intersect around $k = 0.2$, and scenario (1) occurs. The purpose of the green line is to demonstrate that a velocity of 12 m/s would be required for scenario (b) to occur, which is not realistic in Grand Passage. The dashed black line shows the ω_0 value when $V = 0$. The cyan line is tangent to the dispersion relation at $k = 0.4$, and the slope corresponds to $V = 2.45$ m/s, representing case (4), when the group speed is equal to the flow speed and wave blocking would occur. $k = 0.4$ is outside of the range observed during the study period, and so waves with an $\omega_0 = 1$ and $V = 2$ m/s would not be blocked.

2.3 Waves on a Sheared Current

2.3.1 Wave Effects on Vertical Shear

Waves induce mean velocities and modify current profiles. In experiments carried out in a laboratory wave flume, *Kemp and Simons* (1982, 1983) demonstrated increased mean shear in the upper water column with waves opposing the current, and decreased and even reversed sign when with the current. They also demonstrated that the that the magnitude of the effect increased with increasing wave amplitude. Consequently, near-surface currents were increased compared to the no-wave case when the waves and currents were in opposite directions, and decreased when the waves and current were in the same direction. This counter-intuitive result, which will be referred to here as the Kemp-Simons effect, has not been demonstrated in the field.

The Kemp-Simons effect was eventually reproduced in an analytical model by *Groeneweg and Klopman* (1998), as shown in Figure 2.2. The model implemented Generalized Lagrangian Mean (GLM) equations of motion, which allow for the separation of mean and oscillatory motion. *Groeneweg and Klopman*'s GLM theory involved complex algebra, but does not provide a physical mechanism (*Smith*, 2006).

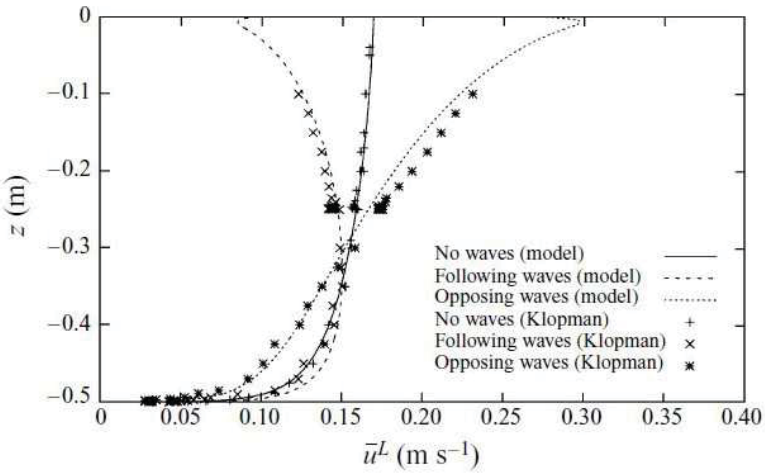

Figure 2.2: Comparison of the *Groeneweg and Klopman* (1998) model to the lab results of *Klopman* (1994). From *Groeneweg and Klopman* (1998)

2.3.2 Effect of Vertical Shear on the Dispersion Relation

Kirby and Chen (1989) derived a perturbation expansion hierarchy for the dispersion relation governing waves on a vertically sheared mean flow. They assumed linear wave theory, with an arbitrary but weak mean velocity such that $|U(z)| << c$, where $c = \omega_0/k$ is the absolute wave phase speed, i.e. with respect to the fixed frame. Their expression for the first order correction to the phase velocity is

$$c_1 = \frac{2k}{\sinh 2kh} \int_{-h}^{0} V(z) \cosh 2k(h+z) dz \equiv \tilde{V} \tag{2.13}$$

so, with $c = c_0 + c_1$, the dispersion relation becomes

$$\omega_0 = \sqrt{gk \tanh kh} + k\tilde{V} \tag{2.14}$$

To illustrate the effect of vertical shear on the dispersion relation, the result obtained by *Stewart and Joy* (1974) for deep water (which *Kirby and Chen* (1989) show is identical to their first-order solution in deep water) is used, i.e.

$$\tilde{V}(k) = 2k \int_{-\infty}^{0} V(z) e^{2kz} dz \tag{2.15}$$

For a linear shear current profile (i.e. uniform shear) in finite water depth (but deep enough that the deep water wave solution is a good approximation)

$$V(z) = V_s \left[1 + \frac{2\alpha z}{h} \right] \tag{2.16}$$

where

$$\alpha = 1 - \frac{V_o}{V_s} \tag{2.17}$$

where V_s is the surface velocity, and V_o is the mid-depth velocity.

Figure 2.3 illustrates the effect of a vertically sheared current on the dispersion relation, for waves both with and against the current. The red line represents positive shear, and the green is negative shear. The predicted effects are clearly much greater for the wave against case, indicating a pronounced increase (decrease) in wavenumber with positive (negative) shear, consistent with what one would expect physically as shoaling effects would increase with velocity.

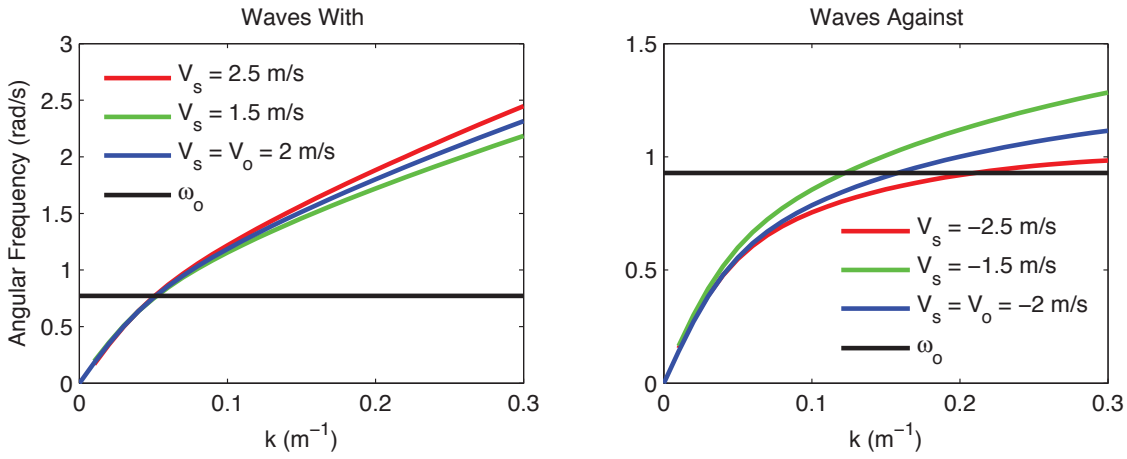

Figure 2.3: Dispersion relation for waves with and waves against a sheared current. The ω_0 reference line shows the observed frequency in Grand Passage on a maximum ebb (waves with) and flood (waves against) tide. The curved lines are angular frequencies that would be obtained for each V_s from Equation 2.14 with $\tilde{V}(k)$ from Equation 2.13.

2.4 Distortion of the Turbulence Spectrum by Wave Motions

The Reynolds number, Re, is the ratio between inertial and viscous in the momentum equations

$$\mathrm{Re} = \frac{UL}{\nu} \tag{2.18}$$

where L represents the length scale, and ν the kinematic viscosity. *Kolmogorov* (1941a,b) predicted that at very high Reynolds numbers, an inertial subrange would exist in which the energy spectrum $E(k)$ would assume a universal form given by

$$E(k) = C\epsilon^{2/3}k^{-5/3} \tag{2.19}$$

where C is a universal constant and ϵ is the dissipation rate.

Lumley and Terray (1983) reported a turbulent velocity spectrum from measurements in

a combined wave-current flow, that exhibited the -5/3 dependence on either side of the wind-wave peak, but also apparent increase in the spectral densities on the high frequency side. This observation led them to develop a kinematic model to simulate the distortion of the mean flow turbulence spectrum in the inertial subrange by wave orbital motions. The model, which invokes Taylor's frozen field hypothesis and assumes linear (i.e. non-breaking) waves, was able to reproduce the observed effects, as indicated in Figure 2.4.

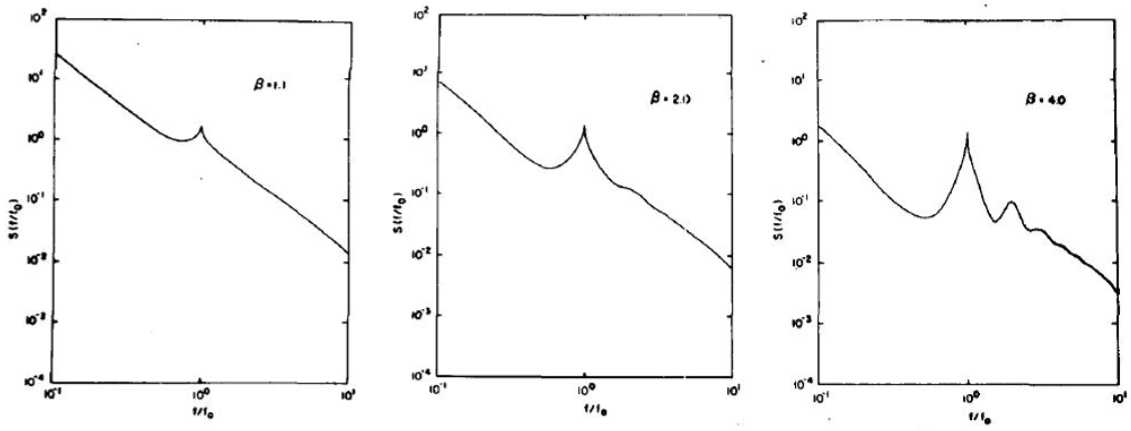

Figure 2.4: The velocity spectra, scaled by a constant $\beta = \omega_0 R/U$, where R is the orbital radius, and U is the drift velocity. The y-axis label is the spectral density, and the x-axis is f/f_o, frequency scaled by peak wave frequency. The β values are 1.1, 2.0 and 4.0 and represent the relative strength of the rms orbital velocity in deep water to the mean current. Taken from (*Lumley and Terray*, 1983).

CHAPTER 3

METHODS AND DATA SET

3.1 Field Site

Grand Passage, shown in Figure 3.1, is located in the southwest Bay of Fundy, Nova Scotia, Canada. It is oriented north-south, with flood tide being from St. Mary's Bay in the south, to the Bay of Fundy in the north. Grand Passage has a maximum width of approximately 1.5 km, and length of approximately 4 km. There is a half-hourly ferry across the width of the channel. CTD measurements at slack, flood and ebb tides indicated that the channel was well mixed with depth with no obvious stratification (*Malinka et al.*, 2015). Grand Passage experiences depth averaged peak flows of over 2.5 m/s (*Hay et al.*, 2013a,b). The bottom is heterogeneous, including bedrock, gravel, shells and coarse and fine sediment. The channel bathymetry is shown in Figure 3.2, with along the channel depth ranging from approximately 10-30 m.

(a) (b)

Figure 3.1: Grand Passage, NS, with waves at North entrance highlighted ©googlemaps

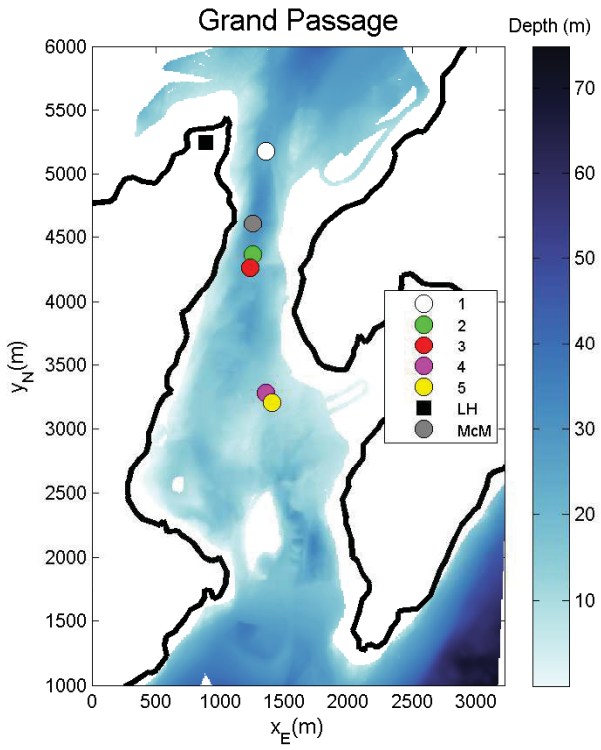

Figure 3.2: Bathymetry of Grand Passage, NS. Instrument locations are (1) AWAC; (2) RDI Pod; (3) Cabled ADCP; (4) ADCP Platform North; (5) ADCP Platform South; (LH) Lighthouse, the location of the Environment Canada weather station. This research used data from the cabled ADCP, with the other four instruments involved in the broader project.(McM) is the location of the ADCP in the work of *McMillan et al*. (2016); *McMillan and Hay* (2017).

3.2 Instrumentation

The instruments involved with the greater project in Grand Passage are shown by location in Figure 3.2. The geographic locations and operating parameters for each instrument are listed in Table 3.1.

Table 3.1: Instruments in Grand Passage

Station	Instrument (deployment–recovery dates)	Lat (°)	Lon (°)	Acoustic Freq (kHz)	Sample Rate (Hz)	Range Res. (m)	Water Depth (m)
1	AWAC (14/03/16–02/04/16)	44.2849	66.3379	1000	2	0.5	24.9
2	RDI Pod (14/03/16–02/04/16)	44.2776	66.3391	600	2	0.5	25.2
3	Cabled ADCP (23/07/16–04/04/16)	44.2767	66.3393	600	2	0.5	23.5
4	ADCP Platform N (8/03/16–02/04/16)	44.2679	66.3378	500	2	0.5	11.0
5	ADCP Platform S (8/03/16–02/04/16)	44.2671	66.3372	500	2	0.5	10.3

Acoustic Doppler Current Profilers (ADCPs) register instantaneous velocities along equally-spaced range bins using the Doppler shift of the received ping. *Terray et al*. (1997) investigated the use of bottom- mounted ADCPs to measure wave heights and direction, and showed that waves observed by the ADCP were comparable to the Field Research Facility's pressure array measurements. The surface, determined using beam echo intensity data, was found to contaminate the time series in the upper- most range bins. Due this contamination and the ADCP tilt, only depth bins below the surface by 25% of the depth were used. The wave height spectrum was calculated from averaged measured velocity spectra at a fixed height above the bottom, using linear theory. Subsequently *Terray et al*. (1999) used bottom- mounted ADCPs to measure waves and currents, and found good agreement between the echo range and velocity- derived wave heights, for frequencies less than 0.35 Hz. Overall wave height and frequency spectra from the ADCP agree with the spectra from a pressure sensor located nearby, as well as other parameters such as peak period, direction and significant wave height.

The ADCP used in this study was located at station 3, and was cabled to a data acquisition system on shore. The ADCP has 4 beams in two orthogonal pairs: the so-called Janus configuration (Figure 3.3). The beam 1-2 plane was oriented approximately east-west, the 3-4 approximately north-south, with beam 3 to the north, and beam 2 to the west. Thus beams 1 and 2 measured linear combinations of across-channel and vertical velocity,

whereas, and beams 3 and 4 registered along-channel and vertical velocity. The coordinate system used here is indicated in Figure 3.3, with z (not shown), positive up. The ADCP transducers were nominally 0.5 m above bottom, with the first measurement bin being 1.6 m above the transducers. The surface return, determined from the backscatter amplitude, was used to determine water depth (and was 1 m less than the mean pressure). In Figure 3.3 positive pitch and roll are indicated, with a positive pitch meaning that transducer 3 is higher than transducer 4, and positive roll that transducer 2 is above transducer 1.

Mid-depth U and V values were averaged in 0.25 m/s speed bins. In Figure 3.3 a linear trend line fit to speed bin averaged U and V velocities indicates the direction in ADCP coordinates. Thus, on the flood tide the flow is 6.25° clockwise from beam 3 (ADCP "north") and on the ebb the flow is 2.99° clockwise from beam 4 (ADCP "south") at mid-depth.

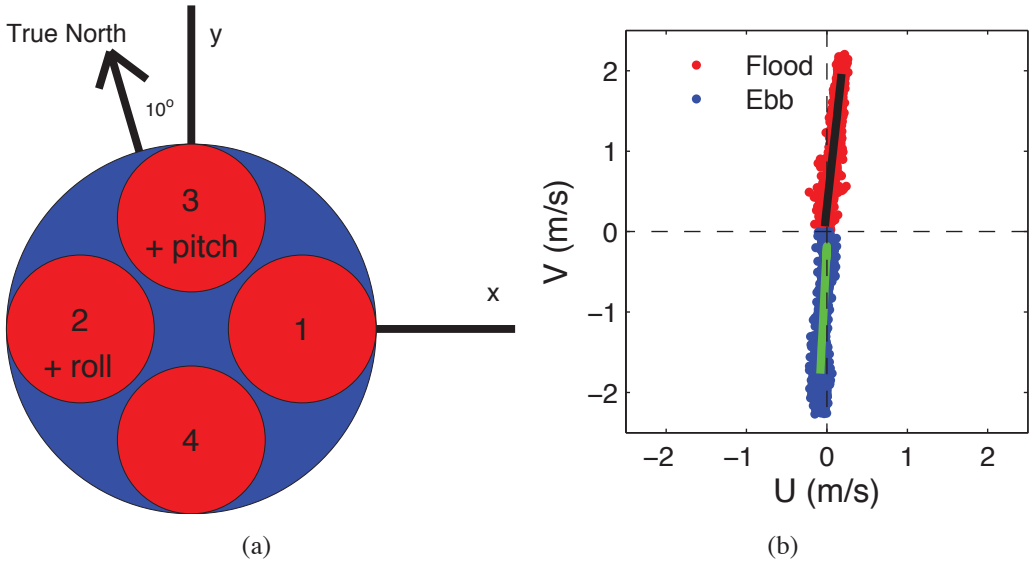

(a) (b)

Figure 3.3: (a) Top view of the ADCP; (b) U and V at mid-depth with trend lines for ebb and flood

3.2.1 ADCP Attitude Stability

The ADCP roll, pitch and heading during the measurement period of interest are presented in Figure 3.4. The average heading was 27.29°±0.11°. The pitch was -1.93°±0.01°, and a roll of -3.76°±0.08°.

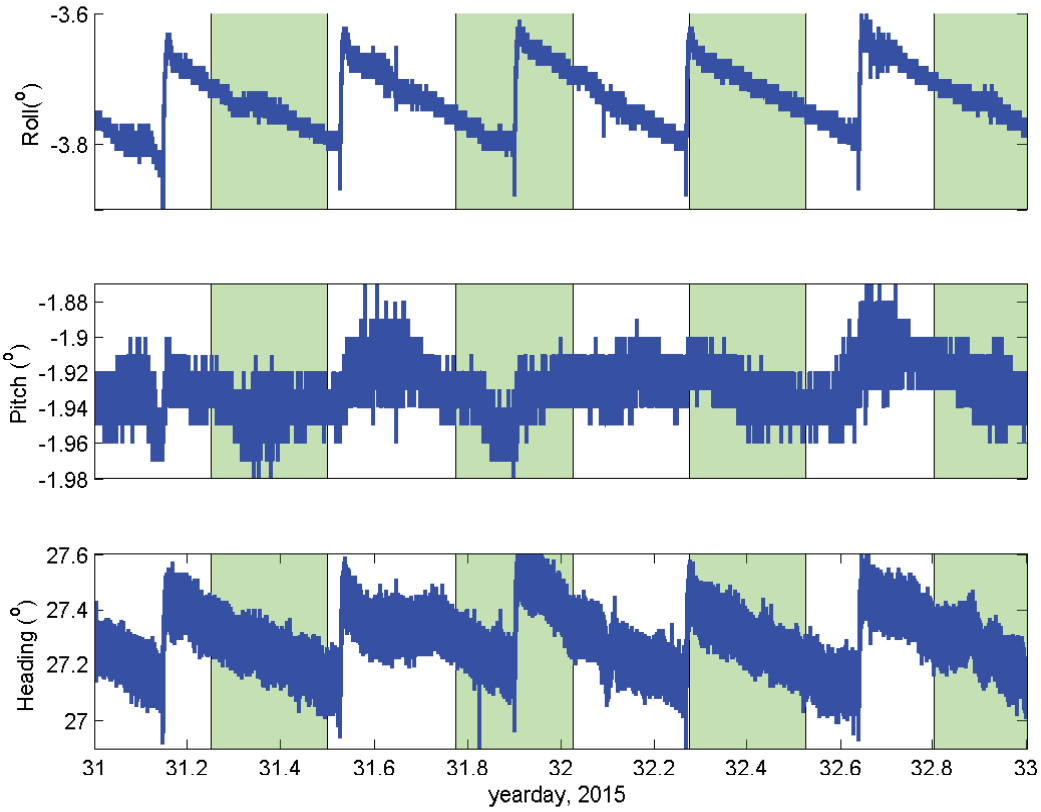

Figure 3.4: Pitch, roll and heading of the ADCP during 2 days of the 10 day storm period in Jan/Feb 2015. Roll is beams 1 and 2 and pitch is beams 3 and 4. The source of the variation in signal is unknown but thought to be due to electrical issues.

3.3 Storm Conditions

The Grand Passage area has average air temperatures ranging from -3° C in January, to 17° C in August. Average wind speeds range from 4.5 m/s in the summer to 6 m/s in winter months, with record wind speeds over 28 m/s. Environment Canada classifies marine wind speeds as ‘strong’ when over 10.2 m/s, ‘gale-force’ when over 17 m/s, ‘storm-force’ when over 24.5 m/s and ‘hurricane-force’ over 33 m/s. Based on records from Environment Canada’s Brier Island weather station (Fig. 3.2), Grand Passage experienced four storm events with winds in the ‘gale-force’ category between July 2014 and July 2015. Three were winter events, occurring between November 2014 and March 2015, and one was Hurricane Arthur in July 2014.

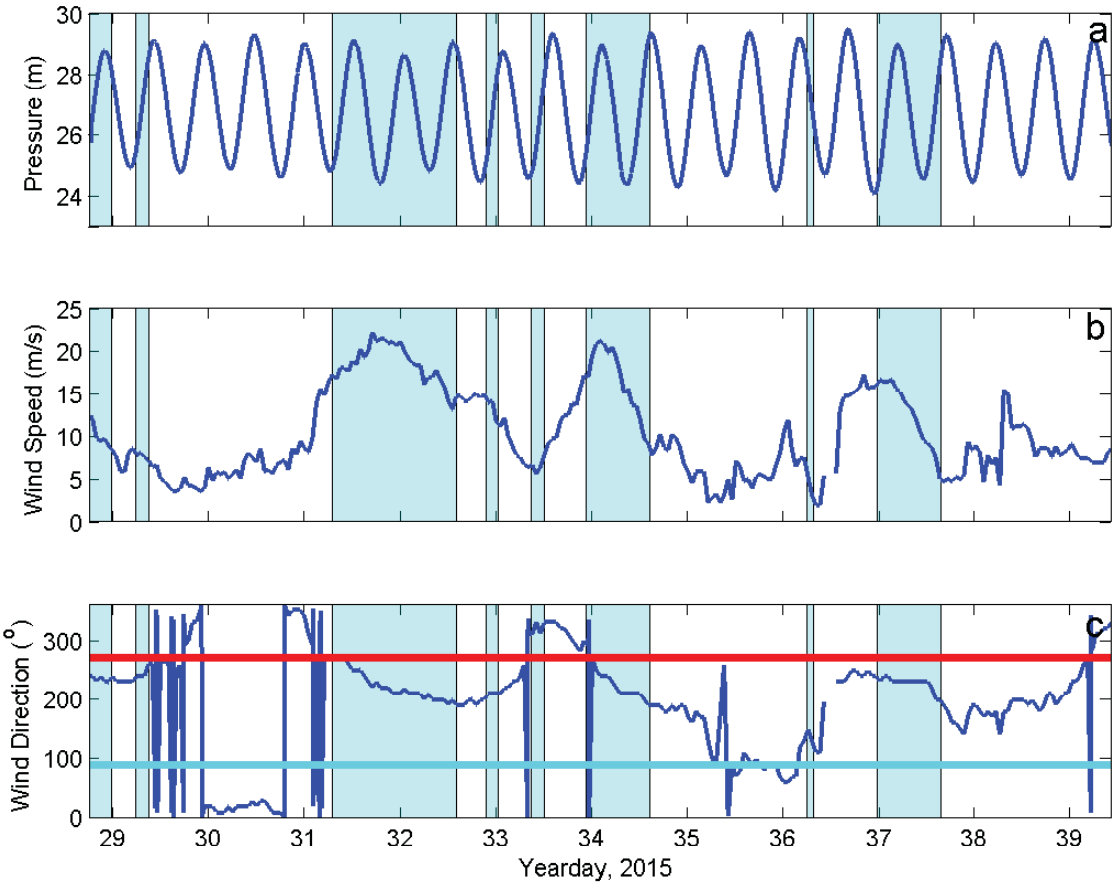

Figure 3.5: (a) Tidal elevation, (b) wind speeds and (c) wind direction. Tidal elevation was derived from the pressure sensor on the ADCP, corrected as indicated in Section 3.4. Wind speed and direction were from the weather station at the North Point lighthouse. Wind directions are clockwise from east, with the red line representing wind from the north, and cyan from the south.

The ADCP deployed had collected over a year of data, and ten days spanning a storm event at the end of January 2015 were selected for analysis based on wind speed, direction and duration, and the orientation of the ADCP. The wind speeds were in the 'gale-force' category for approximately 24 hours on day 32, with maximum wind speeds of 22 m/s. The gale force winds were preceded and followed by 12 hours of 'strong' winds. The wind directions were northerly, varying between 20° and 280°. Thus, wind-generated waves were with the tidal current on the ebb tide, and against the current on the flood. Figure 3.5 shows the time series of tidal elevation, wind speed and direction. The highlighted times are storm events with strong northerly winds. The tidal elevation measurements

were obtained from the ADCP's pressure sensor. The tides in Grand Passage are predominantly M2, with a period of 12.42 hours.

3.4 Pressure Measurements

The pressure signal was noisy (Fig. 3.6). Despite the high noise level, and the attenuation of the wave signal by the 25 m deep water column, it is clear that the high waves on flood tide during storms were detected.

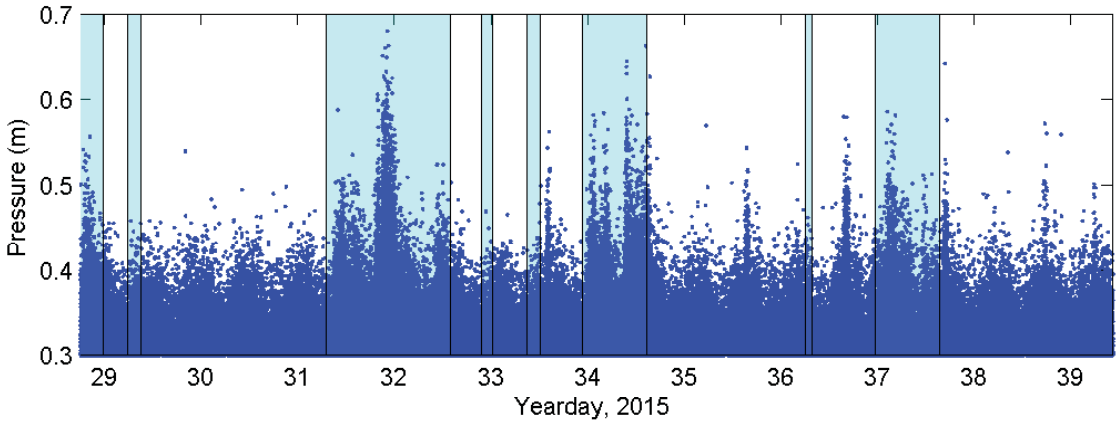

Figure 3.6: Time series of the magnitude of the residual pressure – i.e. the absolute value of ADCP pressure signal after high-pass filtering to remove the tide – with storm times highlighted

CHAPTER 4

DATA PROCESSING

4.1 Wave Frequency

Two measures of wave frequency are used in this thesis. The first is the peak frequency, which was obtained from the peak in the waveband (1/20 to 1/3 Hz) of the 20 minute near-surface beam velocity spectra, S_{ww}. The second is the energy weighted frequency, calculated as

$$f_E = \frac{\int_A^B f S_{ww} df}{\int_A^B S_{ww} df} \tag{4.1}$$

where A and B are the limits of integration, in this case the waveband frequencies.

4.2 Beam Velocity Calculations

The beam velocity, $\hat{v}_j$, is the projection of vertical and horizontal velocity components onto the unit vector parallel to the beam direction. In the RDI convention, beam velocities are positive towards the transducer. Figure 4.1 illustrates the geometry in the across-channel plane.

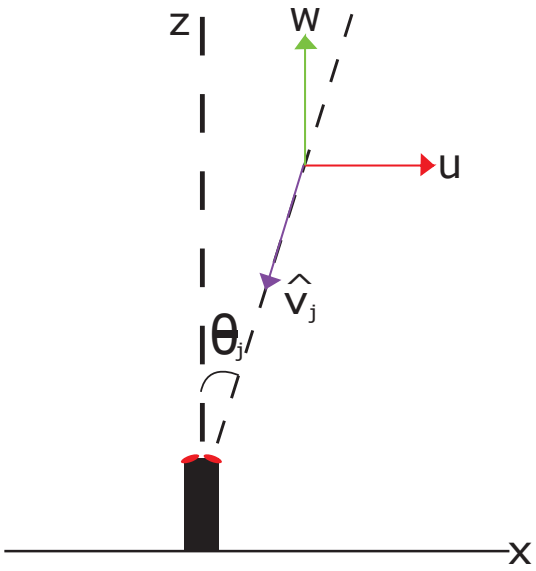

Figure 4.1: The across-channel convention for velocity measurement where θ_j is the angle of the jth beam with respect to the vertical, $\hat{v}_j$ is the beam velocity, and u and w are the horizontal across-channel and vertical velocities respectively.

The beam velocity for the jth transducer is

$$\hat{v}_j = -w \cos\theta_j \pm u \sin\theta_j \tag{4.2}$$

where the choice of sign is positive for transducer 2, and negative for transducer 1 (see Fig. 3.3). There is a corresponding expression for the along-channel beam pair, with v substituted for u. The across-channel flow, u, is given by

$$u = \frac{\hat{v}_2 \cos\theta_1 - \hat{v}_1 \cos\theta_2}{\sin\theta_2 \cos\theta_1 + \sin\theta_1 \cos\theta_2} \tag{4.3}$$

with $\hat{v}_1$ and $\hat{v}_2$ being the along-beam 1 and 2 velocities, and θ_1 and θ_2 being the angle of these beams relative to vertical, accounting for roll: i.e. $\theta_1 = \theta_0 - 3.76^\circ \pm 0.08^\circ$, and $\theta_2 = \theta_0 + 3.76^\circ \pm 0.08^\circ$. The beam velocities were zero-phase filtered using a 5th order Butterworth filter with a low-pass cut-off of 0.05 Hz and a high-pass cut-off of 0.5 Hz (0.2 seconds and 20 seconds) to separate the signal into sub-wave-band and wave-band velocities.

Similarly, along-channel tidal velocity, v is given by

$$v = \frac{\hat{v}_4 \cos\theta_3 - \hat{v}_3 \cos\theta_4}{\sin\theta_4 \cos\theta_3 + \sin\theta_3 \cos\theta_4} \tag{4.4}$$

with $\hat{v}_3$ and $\hat{v}_4$ being the along-beam velocities, and θ_3 and θ_4 being the angle of beam 3 and 4 relative to vertical, accounting for pitch: i.e. $\theta_3 = \theta_0 + 1.93° \pm 0.01°$, and $\theta_4 = \theta_0 - 1.93° \pm 0.01°$.

The vertical component of velocity, w, based on beams 1 and 2, is given by

$$w = -\frac{\hat{v}_1 \sin\theta_2 + \hat{v}_2 \sin\theta_1}{\sin\theta_2 \cos\theta_1 + \sin\theta_1 \cos\theta_2} \tag{4.5}$$

4.3 Using *WavesMon*

WavesMon is a data collection and processing software program supplied by Teledyne RD Instruments (RDI) for computing wave statistics and spectra for upward-looking ADCP data, and was initially used to calculate along-channel velocities and wave heights. The data for this project was in beam coordinates, and the objective was to obtain wave statistics and, at the same time, turbulence in the presence of waves. *WavesMon* was designed to process wave statistics approximately every half hour, and current data every 1-2 minutes. For this project, the data was from 0.5 second sampling, and wave and current data was needed on 5 minute intervals to get at the turbulence, and so *WavesMon* was cumbersome or unable to process the data. Additionally, it is not known if *WavesMon* accounts for vertical shear, which was important at some times in this dataset. For these reasons a methodology was developed using instantaneous beam velocities in the wave-band to calculate the wave parameters.

4.4 Estimating Wave Properties from Beam Velocities

4.4.1 Beam Velocity Cross-Correlation

The lagged cross-correlation function, R_{ij} between the beam velocities was computed estimate the wavenumber. Figure 4.2 shows the lagged cross-correlation function computed from the wave-band beam velocities for both beam pairs. The across-channel beams (1 and 2) exhibit zero lag, indicating that these beams were perpendicular to the wave direction. In contrast, the along-channel beams (3 and 4) exhibit a lag of 3 s, with positive lag indicating that beam 3 leads beam 4 (i.e., waves coming from the north, Fig 3.3). Therefore, for the wave period of approximately 7-8 s, the 3 s lag indicates that the near-surface measurement volumes for beams 3 and 4 were nearly half a wavelength apart, supporting the hypothesis for the WavesMon error. Based on the 3 s lag, and the beam spread of approximately 18 m at the surface, the phase speed, relative to the ground, of these waves would have been approximately 6 m/s.

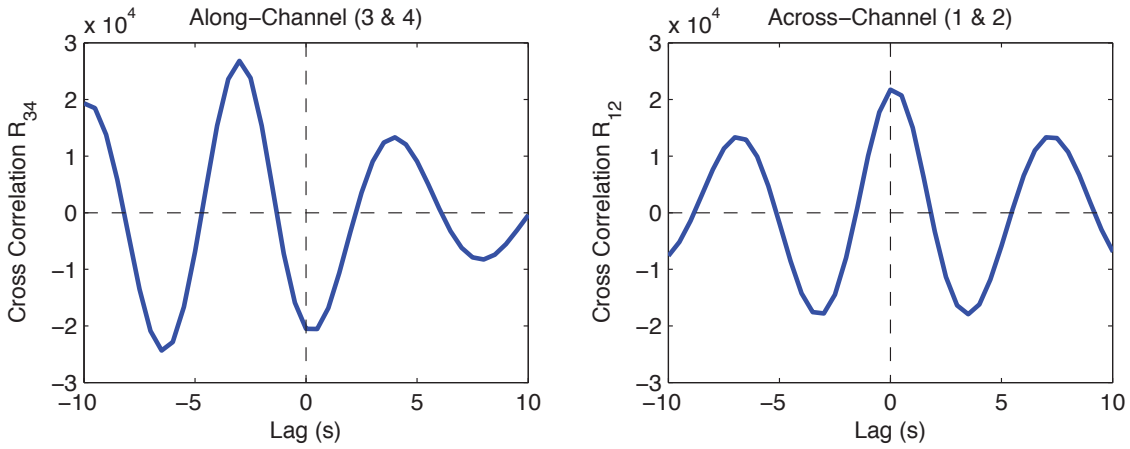

Figure 4.2: Along and across-channel lag between beams near-surface during storm times. There is a 3 second lag for along, and zero lag across.

R_{ij} was computed at 85% of the distance to the surface, to capture the wave signal before the frequency-dependent attenuation influences its spectral content, whilst avoiding the near-surface sidelobe reflection from wave troughs.

For deep water waves, the wavenumber corresponding to the lag, τ, at the peak in the 2-beam correlation function is given by (see Appendix B)

$$kL(z) = \omega_0 \tau(z) - 2\theta \tag{4.6}$$

where ω_0 is the observed frequency in the stationary frame, L is the beam separation and θ is the angle the beams make with the vertical. For this calculation, $\theta = 20^0$, because the angle of the beams is consistent with respect to the instrument, regardless of pitch and roll. Since the lag is discretized in 0.5 s increments, a parabolic fit to five points centred on the peak of R_{34} was implemented to obtain a more precise value of τ.

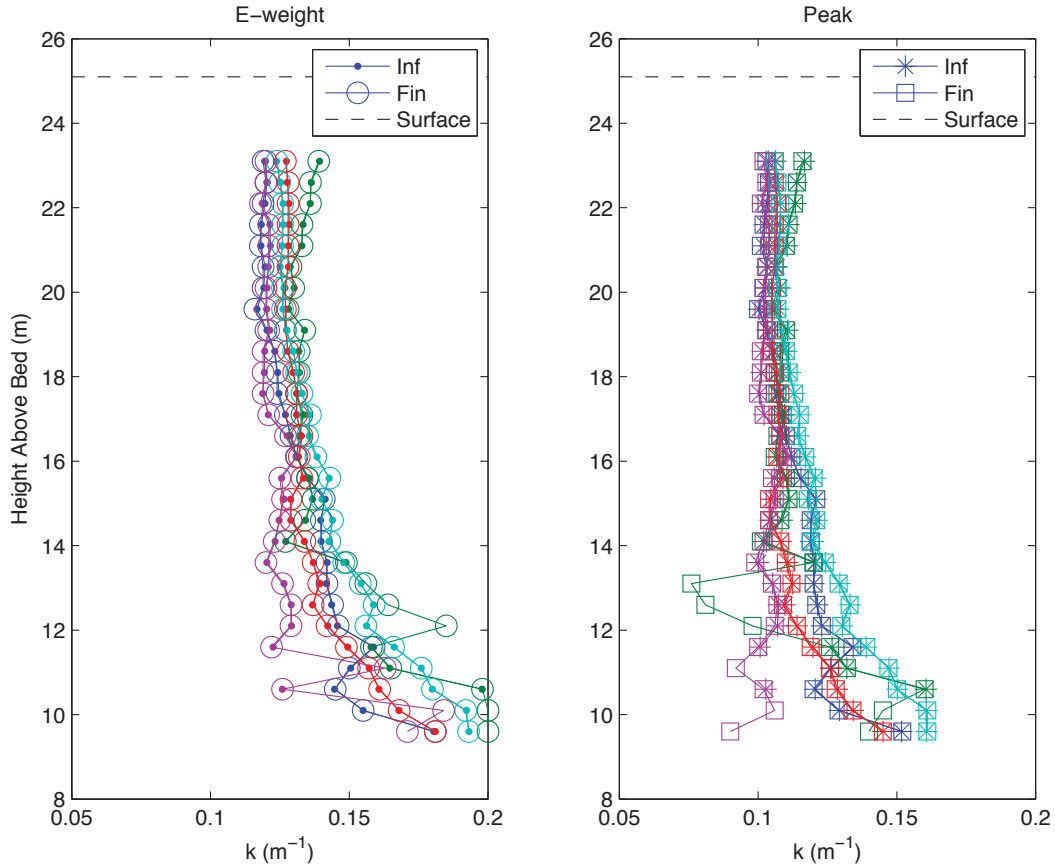

Figure 4.3: Vertical profile of k estimates from beam 3 and 4 cross-correlation function.

Figure 4.3 shows five examples of the vertical profiles of the estimates of k at peak flood during the storm, using both the energy-weighted and peak frequency for ω_0, and both the infinite and finite depth equations. In the upper 10 to 15 m of the water column, the estimates are independent of depth, as expected as they are not influenced by bottom shear stresses.

4.4.2 Vertical Velocity Variance versus Depth

As indicated by Equations 2.2 and 2.3, the decay with depth of wave orbital velocity can in principle be used to provide estimates of wave height and wavenumber.

An example of the vertical profiles of the variance for each of the wave-band beam velocities for transducers 1 and 2, was calculated over 5 minute intervals as shown in Figure 5.5. There is a consistent difference between the two cross-channel beams, with beam 1 biased high compared to beam 2 at equal range. This difference is due to the roll of the instrument. Non-zero roll causes the beam 1 and 2 range bins to be at different depths. The difference in range cell depth due to a 3.76 degree roll (see Figure 3.4) is

$$\Delta z = [\cos(16.3) - \cos(23.7)]r \tag{4.7}$$

where r is the range, i.e. the along-beam distance to a given range cell from the ADCP. At 25 m range Δz is approximately 1 m: i.e. 2 range cells. To correct for this offset, the actual depth at measurement was calculated for each of beams 1 and 2 accounting for the roll, and velocities were interpolated onto these depths. The resulting 5 minute, roll-corrected, wave-band beam velocity variances, σ_1^2 and σ_2^2, are shown in Fig 5.5. These roll-corrected variances were summed together to obtain the vertical velocity variance in the gravity wave band, σ_w^2. Based on Eq. 4.2 for $\hat{v}_j$, the sum of the beam 1 and 2 variances is

$$\sigma_1^2 + \sigma_2^2 = \sigma_w^2(\cos^2\theta_1 + \cos^2\theta_2) + 2\sigma_D^2 + 2\sigma_w'^2 \tag{4.8}$$

where σ_w^2 is the wave variance, σ_D^2 is the Doppler noise, $\sigma_w'^2$ is the variance of the turbulence in the waveband.

The depth-dependence of the vertical velocity variance is predicted by linear theory to be given by

$$\sigma_w^2 = b_1\left[\frac{\sinh^2 b_2(z+h)}{\sinh^2 b_2 h}\right] + b_3 \tag{4.9}$$

where the b's are unknowns to be determined by least-squares fit to the data: b_1 and b_2 are related to wave properties by $b_1 = \frac{a^2\omega^2}{2}$, i.e. the value of velocity variance at the surface, $b_2 = k$, and b_3 is the noise term.

A similar fit was calculated for the combined beam 3 and 4 variances, which include contributions from both σ_v and σ_w. The expression in this case is

$$\frac{\sigma_3^2 + \sigma_4^2}{2} = b_1 \left[\frac{\cosh^2 b_2(z+h)}{\sinh^2 b_2 h} \right] + b_1 \left[\frac{\sinh^2 b_2(z+h)}{\sinh^2 b_2 h} \right] + b_3 \tag{4.10}$$

The wavenumber estimates obtained from beams 3 and 4 are compared to those from beams 1 and 2 in Chapter 5.

4.4.3 Velocity Profiles

To obtain profiles of the Eulerian mean velocity, the along-channel flow was calculated with Equation 4.4 for each 0.5 s sample, and then averaged over 5 minutes for each 0.5 m depth bin, without any filtering of the tidal signal. The results are mean velocity profiles from the first bin (1.6 m above the ADCP, or 2.1 m above the bottom) to within 85% of the distance the surface.

4.4.4 Including Shear

To apply the theory of *Kirby and Chen* (1989), the profiles of the along-channel tidal speed, V,were first extrapolated to the bottom and the surface. The first measurement of velocity was 2.1 m above the bottom, so the extension to the bottom was a linear interpolation between zero velocity at the bottom and the value in the first bin. To extend the profile to the surface, all depth bins above 85% of the distance to the surface were assigned the value at 85%. These velocity profiles were used to calculate the along-channel flow which becomes the velocity component of the Doppler shift term, and a comparison of the $\tilde{V}$ values are compared with mid-depth and depth-averaged V in Figure 4.4. The frequencies from the velocity spectra (both peak and energy weighted) were used to solve for the wavenumber in the dispersion relation. These wavenumbers were then compared to those from the decay of velocity variance.

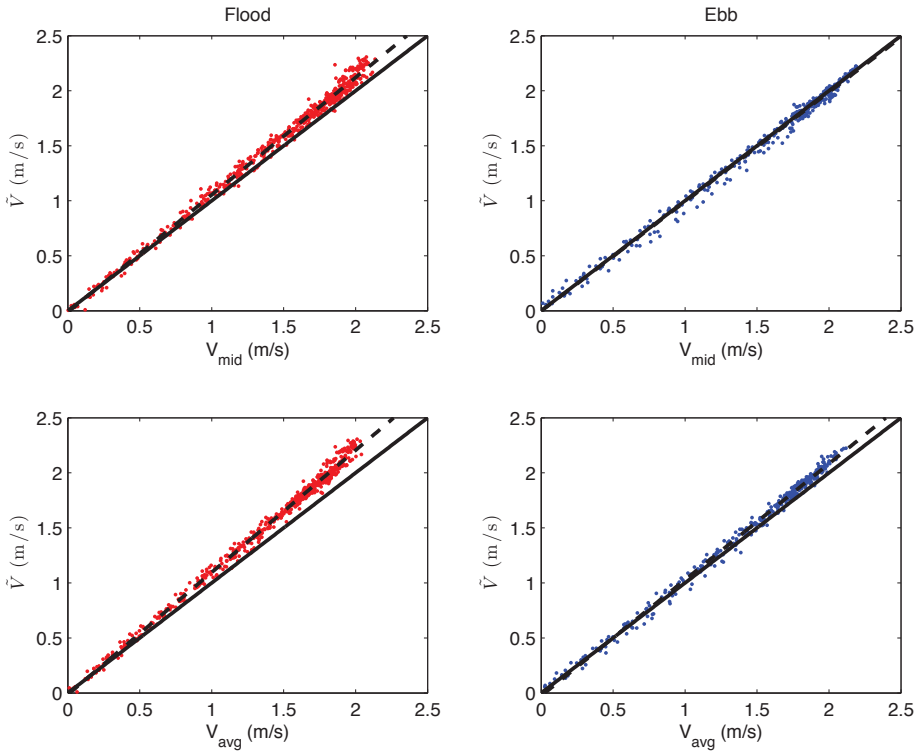

Figure 4.4: Comparing the mid-depth, V_{mid}, and depth-averaged velocities, V_{avg}, with the velocity term which accounts for vertical shear, $\tilde{V}$. Especially on the flood, the velocity term would be increased with the use of $\tilde{V}$. The solid line is 1:1 and the dashed line is the line of best fit.

4.4.5 Quantitative Comparison

To quantify the comparisons of ω for the dispersion relation and wavenumber estimates, the mean squared error (MSE) and R^2 values were used,

$$MSE = \frac{1}{N}\sum(y_i - x_i)^2 \tag{4.11}$$

$$R^2 = \left[\frac{\sum(x_i - \bar{x})(y_i - \bar{y})}{\sqrt{\sum(x_i - \bar{x})^2 \sum(y_i - \bar{y})^2}}\right]^2 \tag{4.12}$$

where x_i and y_i are the wavenumber or ω values on the x and y axis, and $\bar{x}$ and $\bar{y}$ are the mean values of wavenumber. For the R^2 value, the squared 'corrcoef' function in MATLAB can also be used.

CHAPTER 5

RESULTS

5.1 Mean Velocity Profiles

Profiles of the 5 minute averaged along-channel velocity, V, were generated for comparison with the work of *Groeneweg and Klopman* (1998) in Figure 5.1 for both peak ebb and peak flood. Throughout this section, classification is by $2\sigma_w$, a proxy for the wave height, where σ_w is the value at the surface from the fit to the vertical velocity variance decay.

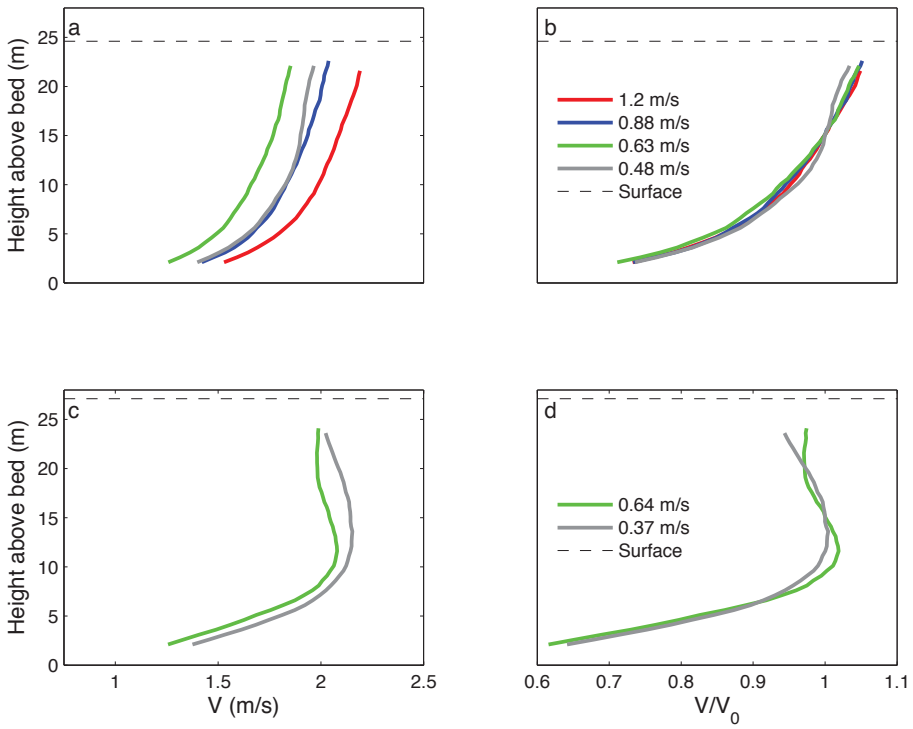

Figure 5.1: Five minute average tidal velocity, V, profiles for each case: (a) maximum flood; (b) maximum flood scaled by mid-depth velocity V_0; (c) maximum ebb; (d) maximum ebb, scaled by V_0. The values in the legend are $2\sigma_w$. Measurements begin at the first bin (1.6 m above the ADCP, or 2.1 m above the bottom), and continue until 85% of the distance between the bottom and the surface.

Figure 5.2 shows when during the 10 day study period the profiles were selected, aiming to represent the range of wave heights present, at times of lower wind speeds, to minimize the effects of wind stress on the velocity profile. The range of $2\sigma_w$ values is greater for flood, simply because on the ebb tide, the wave amplitudes were reduced.

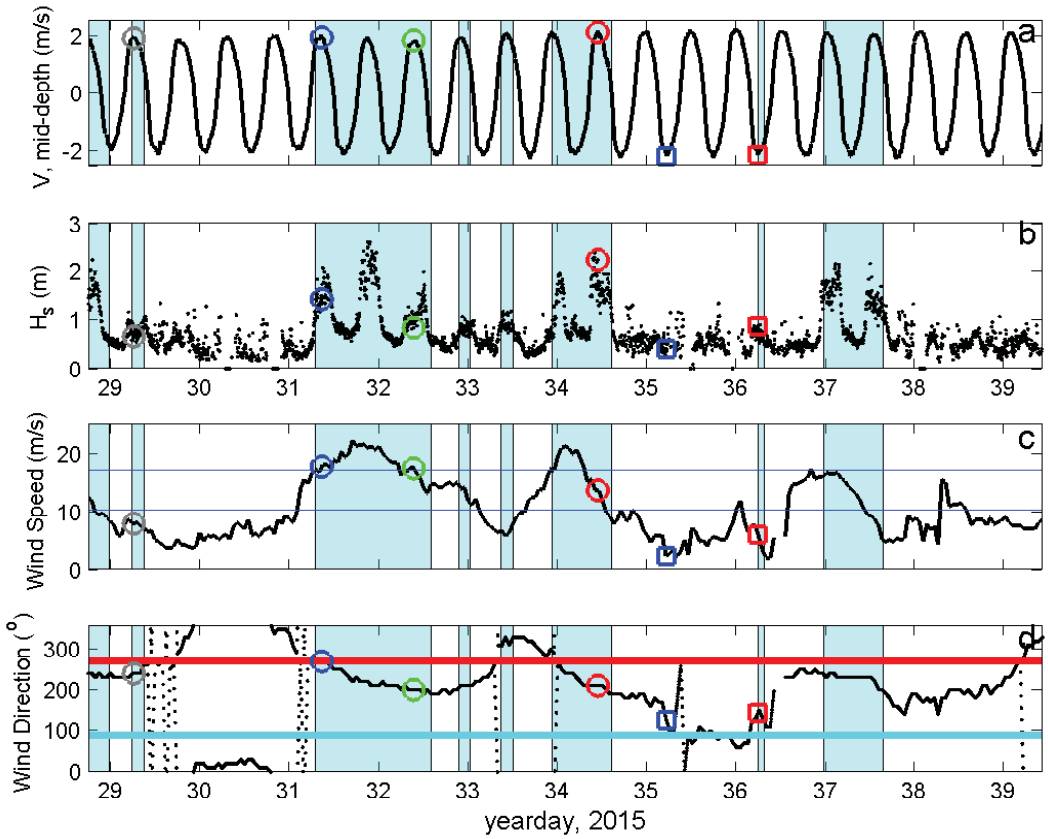

Figure 5.2: Times when the four profiles in Figure 5.1 were taken, with circles for the flood and squares for the ebb. The reference lines in (c) are the thresholds for 'Strong' wind (20-33 kts) and 'Gale-Force' (34-47 kts), as defined by Environment Canada for marine wind conditions. The wind direction in (d) is with respect to east, i.e. the red line represents wind from the north, and the cyan are winds from the south.

The ebb/flood differences between the V profiles are qualitatively consistent with the Kemp-Simons effect: i.e. higher surface speed and near-surface shear when waves and currents are opposed (flood); lower surface speed and tendency toward reversed vertical shear in the upper water column when the current and waves are in the same direction (ebb). However, there is no obvious dependence of these ebb/flood differences on wave height, which would have been expected if they were due to the Kemp-Simons effect.

It is suggested therefore that the observed ebb/flood asymmetry in vertical shear at this location in Grand Passage is due to other dynamical effects.

5.2 Peak vs Energy-Weighted Mean Frequency

Beams 1 and 2 (across-channel) were used to calculate the vertical velocity component at the near surface. The peak and energy-weighted frequencies were calculated for each 20 minute spectra. One 20 minute example during peak flood and ebb during storm conditions, normalized by the velocity variance, is shown in Figure 5.3.

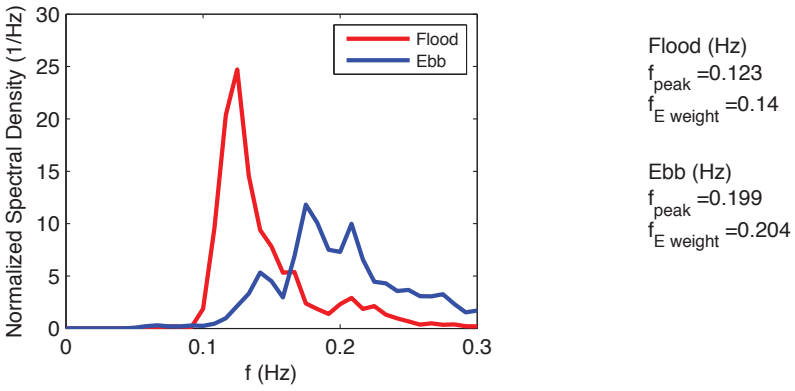

Figure 5.3: Vertical velocity spectra at the near-surface examples for 20 min at the peak of a flood and ebb during storm conditions, normalized the velocity variance. The narrower spectra on flood than ebb is thought to be related to the potential of wave blocking, illustrated in Figure 5.11.

Figure 5.4 compares the peak and energy-weighted frequencies derived from the 20 min velocity spectra throughout all highlighted storm events in the 10 day study period. These frequency estimates are consistent with *Forristall* (1981)'s values of approximately 0.1 to 0.15 Hz for the peak wind wave frequency during wind speeds of 22.4-24.6 m/s. On the flood, there are values of $2\sigma_w$ over the full range, whereas the ebb is dominated by the lowest values. This is due to the fact that there are higher waves on the flood (when the waves oppose the current) than the ebb, which is in agreement with *Dean and Dalrymple* (1991)'s shoaling theory.

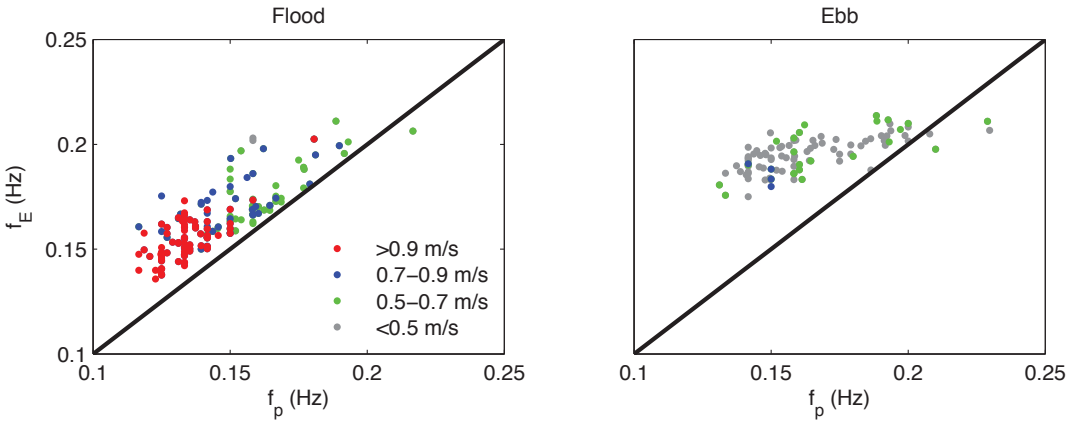

Figure 5.4: Comparison of peak and energy-weighted frequencies from the velocity spectra. Values in the legend are $2\sigma_w$, with larger values corresponding to times with larger wave heights.

The velocity spectrum was calculated for 5 or 20 minute segments, because stationarity could be assumed (i.e. the tide remained constant or changed linearly with time). The 20-minute spectra were used to obtain estimates of the peak and energy-weighted mean frequencies, while the 5-minute spectra were used to compare in log space to the $f^{-5/3}$ line of *Kolmogorov* (1941a,b) and the work of *Lumley and Terray* (1983).

5.3 Estimating Wavenumber

Three independent methods were used to estimate the wavenumber, the degree of agreement representing a test of the applicability of linear wave theory to the wave/current conditions in this data set.

The first method is based on the decay of the 5-minute vertical velocity variance from beams 1 and 2: i.e. from Equation 4.9,

$$\sigma_w^2 = b_1 \left[\frac{\sinh^2 k_{12}(z+h)}{\sinh^2 k_{12} h} \right] + \sigma_N^2 \tag{5.1}$$

This estimate is independent of the observed wave frequency and mean flow speed.

The second method is based on the lag, τ, at the maximum beam 3-4 correlation function $R_{34}(\tau)$ function. As shown in Appendix B τ and k are related in deep water ($kh > 1.75$) by,

$$k_{34}L(z) = \omega_0\tau(z) - 2\theta \tag{5.2}$$

The estimates of k from this method are independent of the mean flow but do require knowledge of ω_0.

The third method is based on the dispersion relation for waves on a current,

$$\omega_0 = \sqrt{gk_E \tanh k_E h} + k_E V \tag{5.3}$$

This method requires both the observed frequency ω_0, and the mean flow speed, V. Note that when accounting for vertical shear, V is replaced by $\tilde{V}$ via Equation **??**.

5.3.1 k from Vertical Velocity Variance Decay

Two examples of 5-minute waveband variance profiles are presented in Figure 5.5, together with the fits to Equation 5.1. These example profiles are high and low σ_w^2 cases. It is evident that accounting for the noise term improves the fit to the decay, which in turn will yield a more accurate estimate of wavenumber. For comparison, the fit was also calculated for beams 3 and 4. Figure 5.6 shows the comparison of the b_1 and k values from the two fits. Since the values are distributed along the 1:1 line, it is concluded that the estimates from beams 1 and 2 are sufficient.

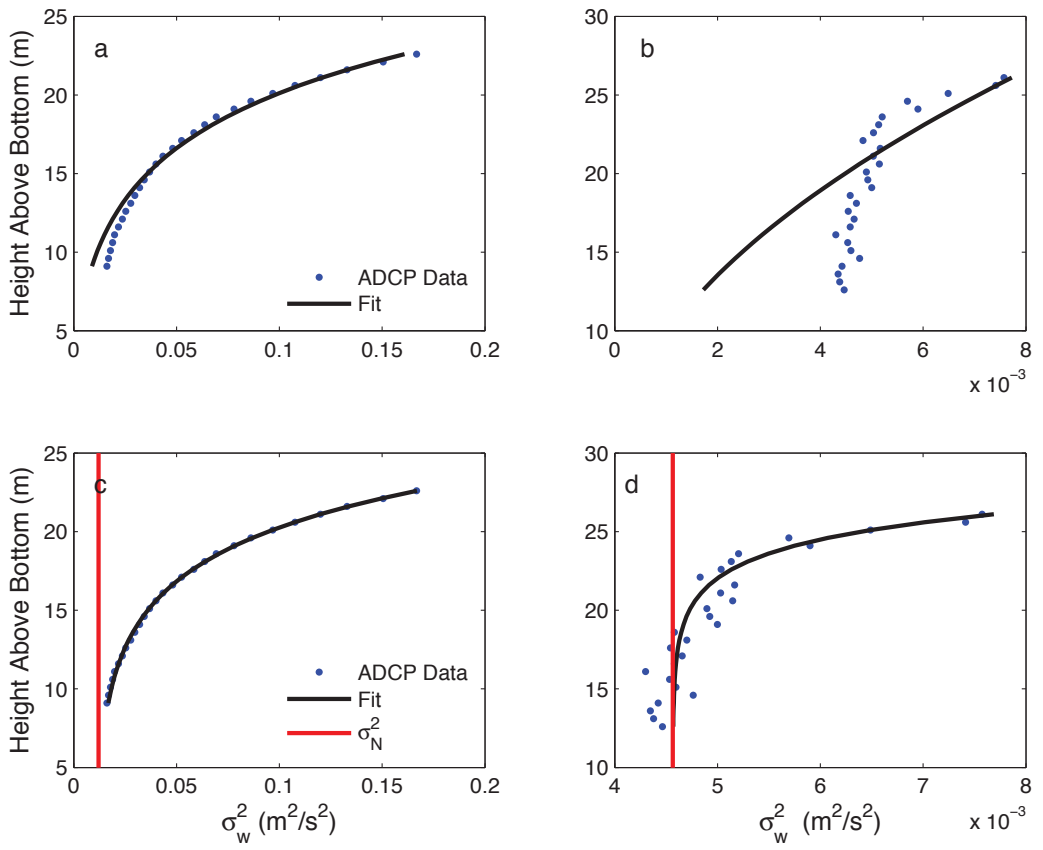

Figure 5.5: Fit to the wave variance decay: (a and c) high wave variance, yd 31.89; (b and d) low wave variance, yd 30.49. The noise term was included in the fits in panels (c) and (d), but not those in (a) and (b).

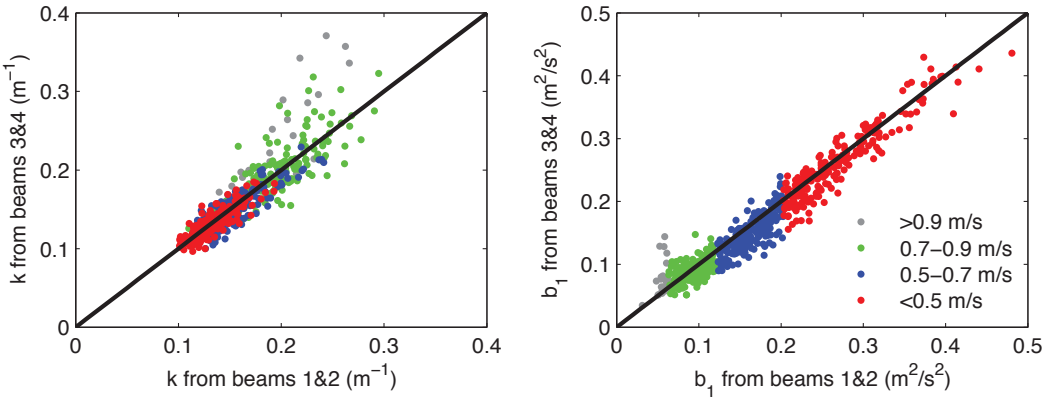

Figure 5.6: Comparison of wavenumber, k, and $b_1 = \frac{a^2\omega^2}{2}$ for the across and along-channel beam pairs of velocity variance decay on flood tide.

The values of k obtained from the fit to the decay from Equation 4.9 are used to calculate

the intrinsic frequency, which is compared in Fig 5.7 to both the peak and energy-weighted mean frequencies for ω_0 from the velocity spectra. The colours represent different ranges of $2\sigma_w$, as indicated in the legend.

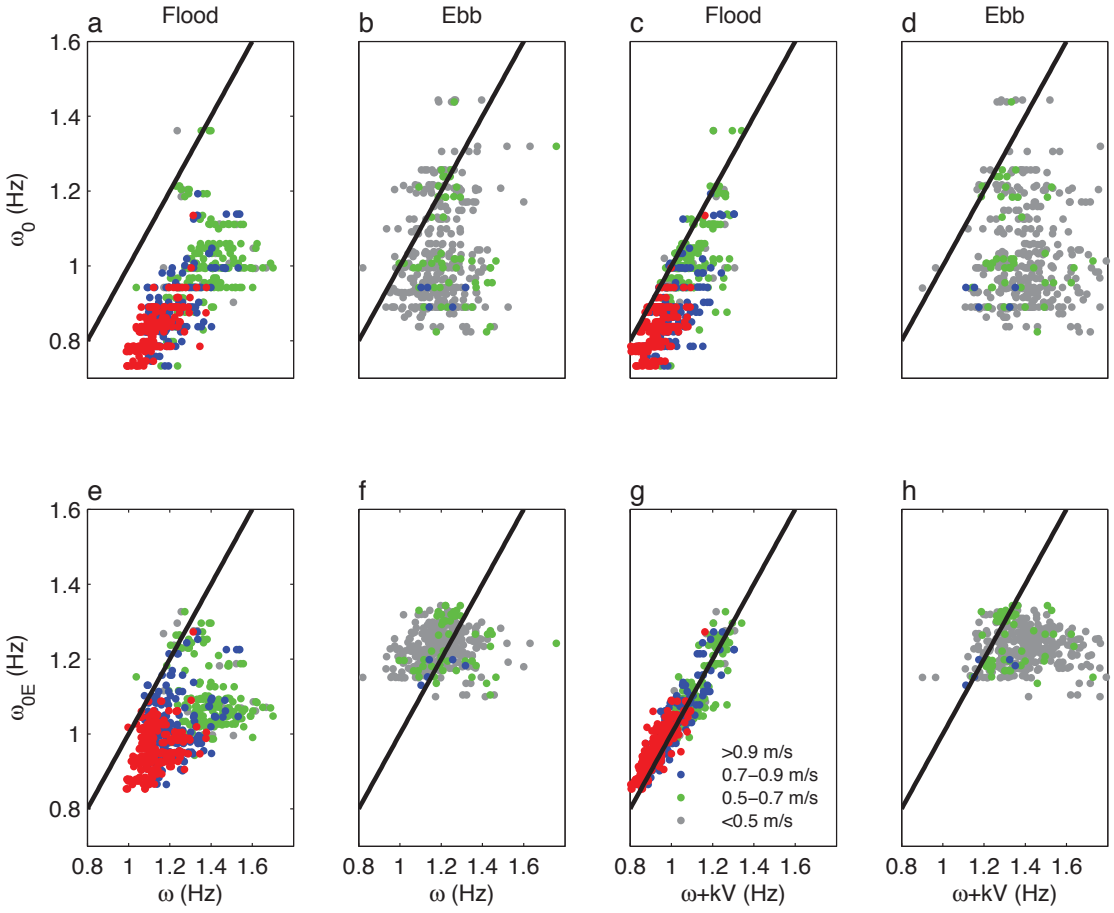

Figure 5.7: Comparing the dispersion relationship with estimates of k from the decay of the vertical variance to the observed frequency from the peak (a-d) and energy weighted (e-h) period. Subplots c,d,g and h include the Doppler shift term. Values in the legend are $2\sigma_w$. ω_0 and ω_{0E} are the observed angular frequencies from the peak and energy weighted frequency respectively, and $\omega = \sqrt{gk \tanh kh}$. V is the mean speed at 12.6-14.6 m above bottom.

	No Doppler		Doppler Shifted	
	Flood	Ebb	Flood	Ebb
MSE (Hz)				
ω_P	0.12	0.055	0.015	0.19
ω_E	0.064	0.017	0.0021	0.067
R^2				
ω_P	0.50	0.034	0.60	0.0035
ω_E	0.22	0.033	0.84	0.0007

Table 5.1: Mean square error (MSE) and R^2 values for the comparisons of the dispersion relation, corresponding to Figure 5.7. ω_P and ω_E are the observed peak and energy-weighted mean frequencies, respectively.

It is evident that agreement between the observed and theoretical frequencies improves with the use of the energy-weighted mean frequency, though quantitatively the R^2 values and MSE on the doppler-shifted flood indicate otherwise. On the flood tide, when waves and currents are opposed, the agreement improves with the inclusion of the Doppler term. On the ebb, however, the agreement appears slightly better without the Doppler term.

5.3.2 k from Beam Correlation

Estimates of k were made using the second method, i.e. from Equation 5.2, using both the peak and energy-weighted mean frequencies. Figure 5.8 compares these estimates of k on both ebb and flood tides to those estimates from variance decay.

Agreement between the estimates of k_{12} (from the variance decay) and k_{34} (from the beam correlation) improved when the k_{34} derived from the energy-weighted mean frequency was used. Quantitatively, on both flood and ebb the MSE decreased and R^2 increased with the use of the energy-weighted mean frequency It is important to note that k_{12} does not rely on the estimate of ω_0, whereas the k_{34} does.

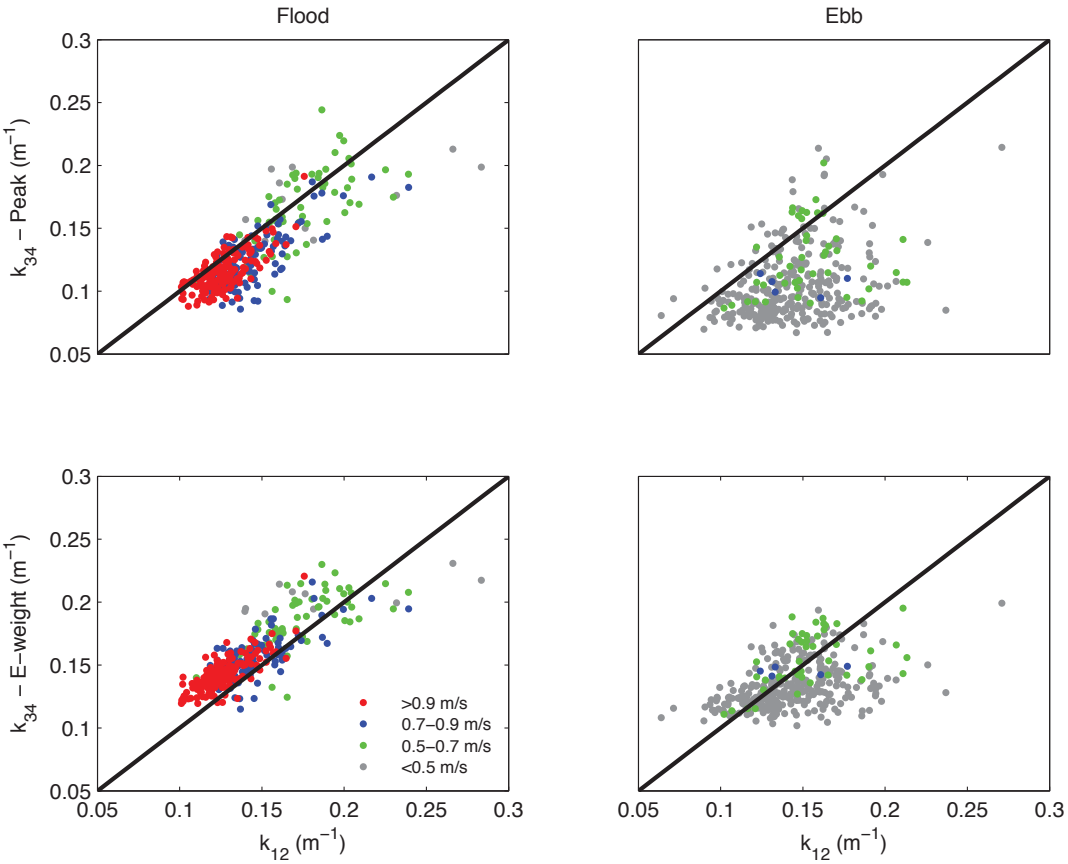

Figure 5.8: Comparing estimates of k_{34} from the beam correlation to k_{12} from the decay of vertical velocity variance on both flood and ebb, from peak and energy-weighted mean frequencies.

	Flood	Ebb
MSE (m^{-1})		
ω_P	0.0035	0.023
ω_E	0.0032	0.0069
R^2		
ω_P	0.67	0.10
ω_E	0.70	0.19

Table 5.2: Mean square error (MSE) and R^2 values for the comparisons of k values from the beam correlation and vertical velocity variance decay, corresponding to Figure 5.8. ω_P and ω_E are the observed peak and energy-weighted mean frequencies, respectively.

5.3.3 k Accounting for Shear

Kirby and Chen (1989)'s theory was used for the velocity term when solving the dispersion

relation, and then was compared with estimates from the decay of velocity variance. The velocity profiles used were the 5-minute mean velocities from Figure 5.1, extended to the bottom and the surface, as outlined in Section 2.3.2.

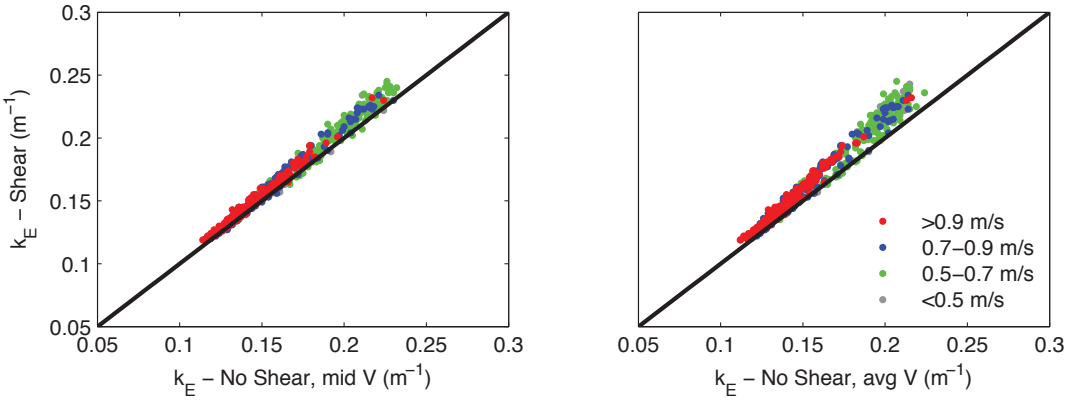

Figure 5.9: Comparison of k including and excluding shear on flood tide for different cases of $2\sigma_w$ in storm conditions. The no-shear cases uses either the mid-depth velocity or vertically averaged velocity, which are very similar.

A comparison of k_E estimates using *Kirby and Chen* (1989)'s first order theory compared to those from the decay of vertical velocity variance is shown for both flood and ebb in Figure 5.10. Agreement between k_E and k_{12} improved with the inclusion of shear, and with the use of the energy-weighted mean frequency, however quantitatively the MSE increased on flood, and on both flood and ebb the R^2 decreased. The agreement between estimates of k_{12} with both k_{34} in the previous section and k_E, supports the use of the values of k from variance decay for estimating wave height.

Figure 5.11 is similar to Figure 2.1, demonstrating the impact of a vertically averaged or sheared current on 5, 10 and 15 second waves. The increased velocity term of the sheared case on 5 second waves demonstrates the potential that wave blocking occurs in Grand Passage. This would explain the lack of higher frequency waves in the velocity spectra during storm times.

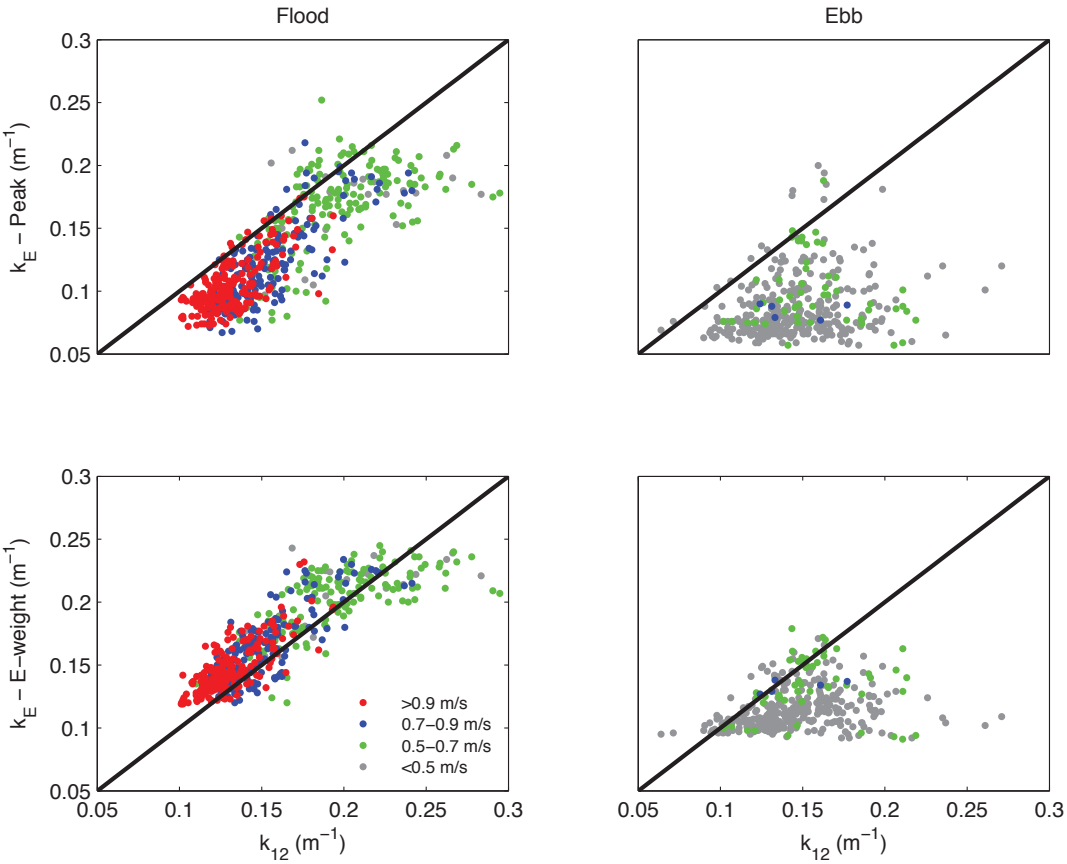

Figure 5.10: Comparing peak and energy-weighted mean frequency estimates of wavenumber from *Kirby and Chen* (1989) and the vertical velocity variance decay on flood and ebb for different cases of $2\sigma_w$ in storm conditions.

	Flood	Ebb
MSE (m^{-1})		
ω_P	0.0014	0.0048
ω_E	0.0005	0.0019
R^2		
ω_P	0.69	0.048
ω_E	0.75	0.056

Table 5.3: Mean square error (MSE) and R^2 values for the comparisons of k values from the accounting for vertical shear in the dispersion relation and vertical velocity variance decay, corresponding to Figure 5.10. ω_P and ω_E are the observed peak and energy-weighted mean frequencies, respectively.

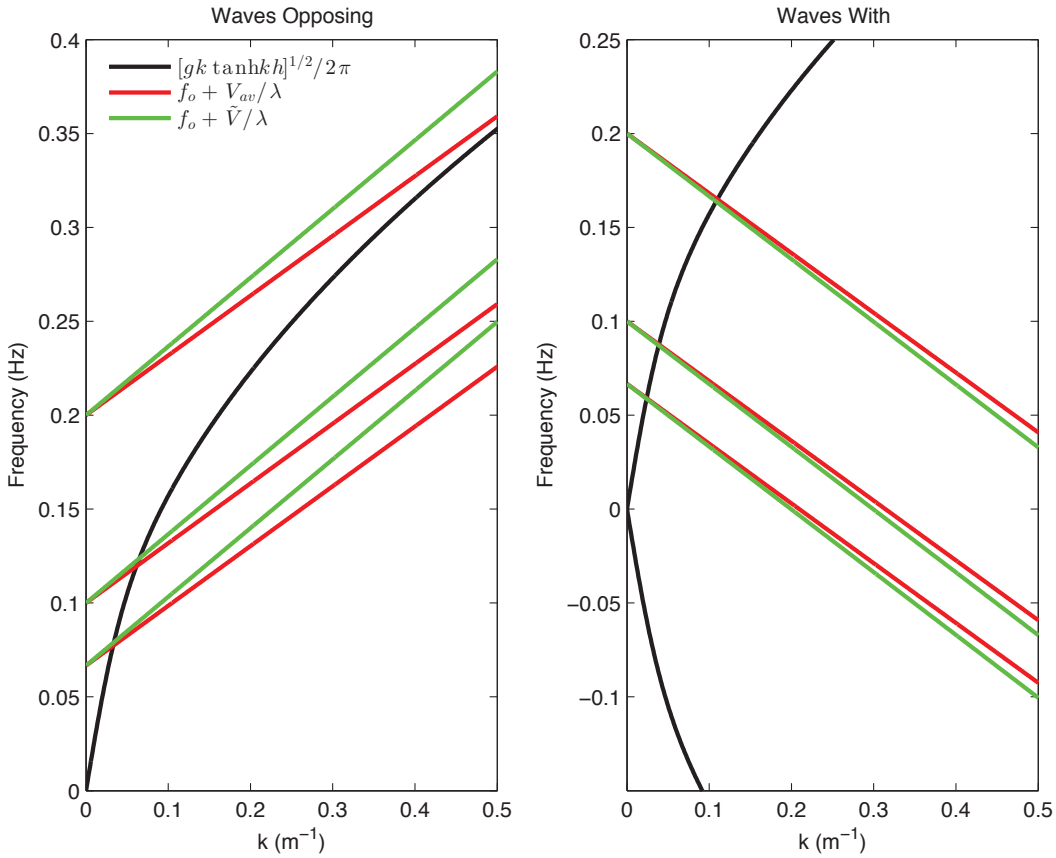

Figure 5.11: Similar to Figure 2.1, this figure demonstrates the impact of a vertically averaged (2 m/s) or sheared (2.3 m/s) current on 5, 10 or 15 second waves on for both waves with and waves against. When the $f + V/\lambda$ term is tangential to the intrinsic curve, group speed is equal to phase speed and wave blocking occurs.

5.4 Significant Wave Height from Velocity Variance Decay

Significant wave heights (H_s) were calculated from the decay of velocity variance with depth. For the calculation of H_s, at $z = 0$, $\sigma_w^2 = b_1$. Figure 5.12 shows the tidal (along-beam 3 and 4) velocity at mid-depth (averaged between 12.6 and 14.6 m above bottom), the pressure time series, the significant wave height derived from Equation 2.8, as well as wavenumber. Stormier time periods with higher wave heights and wavenumbers that do not rapidly change are highlighted as times of interest.

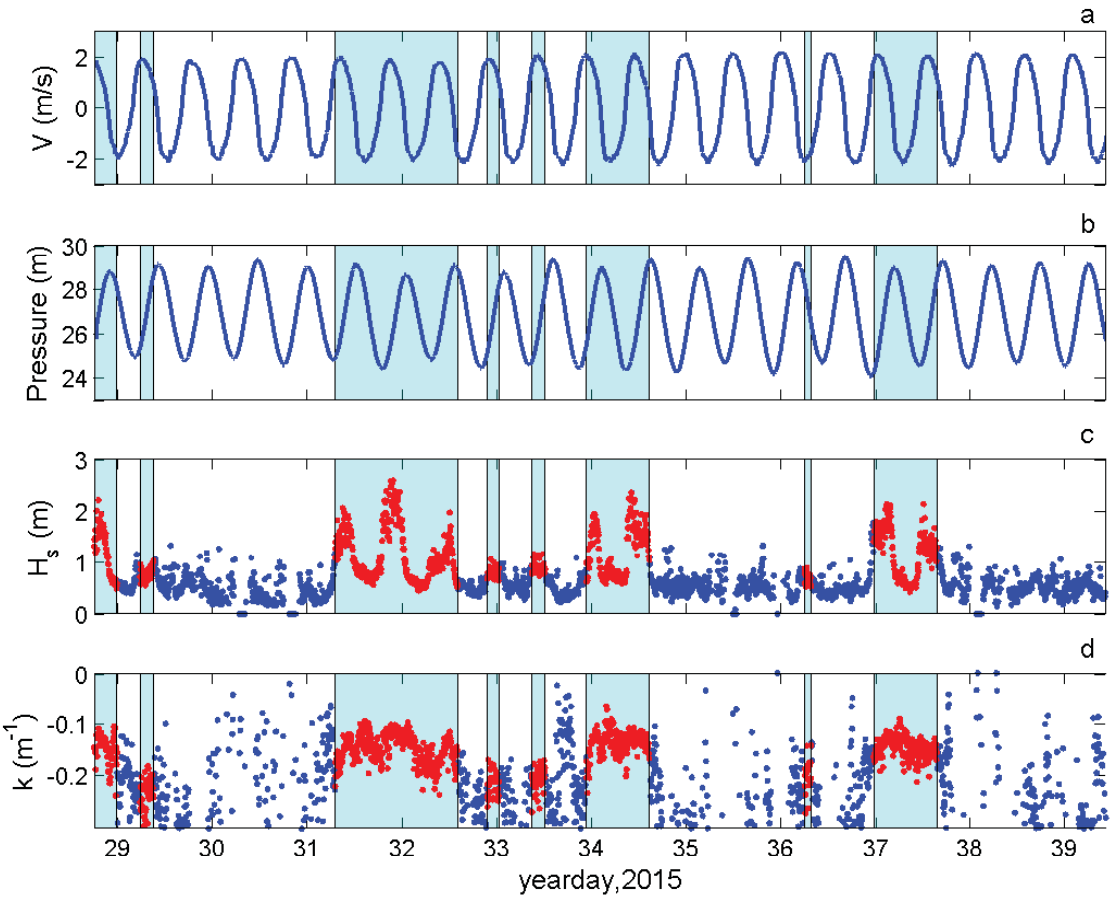

Figure 5.12: (a) mid-depth along-channel velocity; (b) pressure; (c) significant wave height; (d) wavenumber. Cyan highlighting indicates stormier periods. H_s and k are from the decay of velocity variance.

Figure 5.12 demonstrates that significant wave heights are tidally modulated, reaching maximum values of approximately 2-2.5 m during flood tide (i.e. when wave and current directions were opposed). The highest wave heights occurred during the time of strongest wind from the north. The wavenumber increased on the flood tide, and decreased on the ebb, as expected from wave shoaling theory of *Dean and Dalrymple* (1991).

Figure 5.13 shows a comparison of the wave heights estimated from values from the decay of velocity variance, with another estimate that used k_E from *Kirby and Chen* (1989) and σ_w from the value at the surface from the decay method. Both estimates of H_s use the vertical velocity variance at the surface as estimated from the fit to Equation 4.9. The respective wavenumbers estimated for decay from Equation 4.9 and for the shear-corrected,

energy weighted value from Equation 2.14 were then used in Equation 2.8 to calculate H_s.

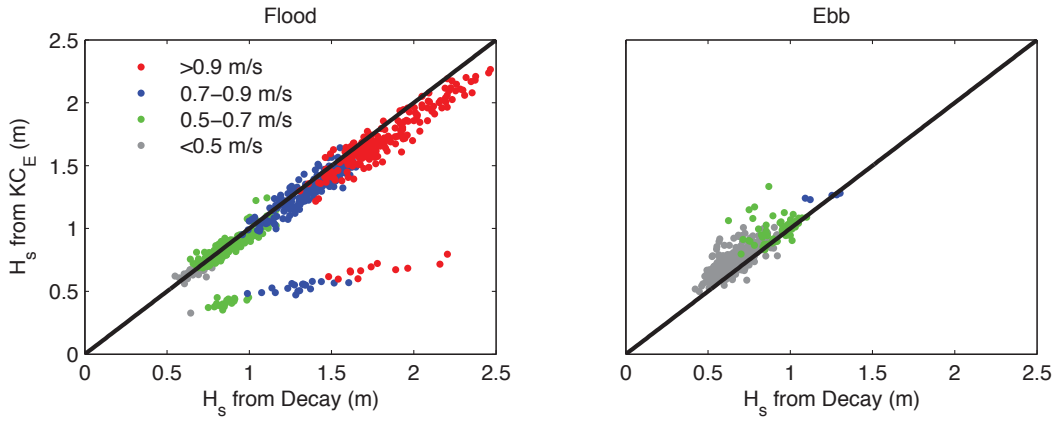

Figure 5.13: Comparing wave height estimates from the decay of vertical velocity variance with those with k from *Kirby and Chen* (1989) on flood and ebb during storm times. The legend values are $2\sigma_w$.

As with estimates of k, there is generally good agreement between estimates of H_s during storm conditions. On the flood there were some outliers when estimates of H_s from the decay were less than those from with k from *Kirby and Chen* (1989).

For comparison, the theoretical maximum wave heights were estimated to be approximately 2.7 m from an empirical formulae for wind waves (Appendix C) using Jonswap parameters as outlined in *Kamphuis* (2000). The fact that this estimated wave height is larger than that shown in the preceding figures can be explained as a result of the formulae being developed for open ocean conditions uninfluenced by bathymetry, land forms or mean currents.

5.5 Significant Wave Height from Pressure

The ADCP's pressure sensor measurements were also used to obtain estimates of k and H_s, to compare to those from velocity measurements. Figure 5.14 shows the 20-minute pressure and velocity spectra (normalized by the variance) at the same maximum of a flood and ebb flow during the storm time as Figure 5.3. The peak and energy-weighted

frequencies are indicated. For the pressure, the energy-weighted frequency is calculated from the denoised spectra.

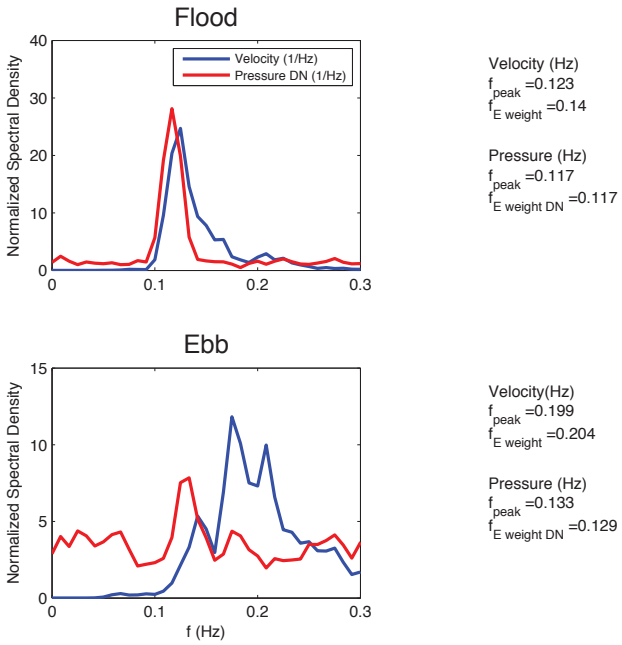

Figure 5.14: Comparison of the normalized near-surface velocity and bottom pressure spectra for the same 20-minute storm segments during peak flood and ebb flows.

The peak and energy-weighted frequencies from the pressure sensor were estimated for the storm times during the 10 day period, and are compared in Figure 5.16. They are the same, on average, because the high-frequency wave signal has been filtered out by the water column, making the spectra very narrow. *Townsend and Fenton* (1996) proposed a pressure response factor to demonstrate the damping of waves with

$$K_p = \frac{\cosh kh_p}{\cosh kh} \tag{5.4}$$

where K_p is the pressure response factor, h_p is the height of the pressure sensor above bottom and h is the mean water depth. Similarly, a vertical velocity response factor, K_w, can be obtained where h_p is the near-surface value. Figure 5.15 demonstrates the effect of damping of the high frequency waves.

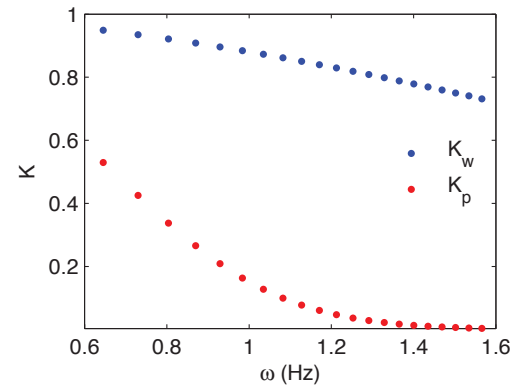

Figure 5.15: Pressure and velocity response factors as a function of frequency, demonstrating the damping of the high frequency waves when using the pressure sensor.

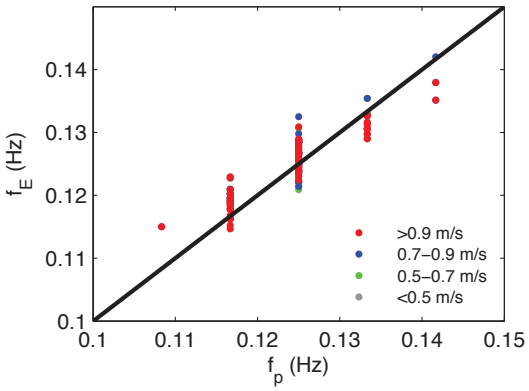

Figure 5.16: Comparing peak and energy weighted frequency from the pressure spectra.

Wavenumber was also estimated from the pressure spectra. Values of this wave number, designated k_p, were needed to estimate H_s in storm conditions when the wave signal rose above the sensor noise floor (Figure 3.6). Figure 5.17 compares the values of k during storm times estimated from velocity variance decay, with those from the velocity and pressure spectra with *Kirby and Chen*'s $\tilde{V}$ equation.

Using the energy weighted frequency value improves the agreement to the k_{12} from decay for both k_E from velocity and k_P pressure. Values of k are consistently lower from pressure estimates than from the velocity decay, as expected because of the shift to lower frequencies due to the low-pass filtering effect of water column.

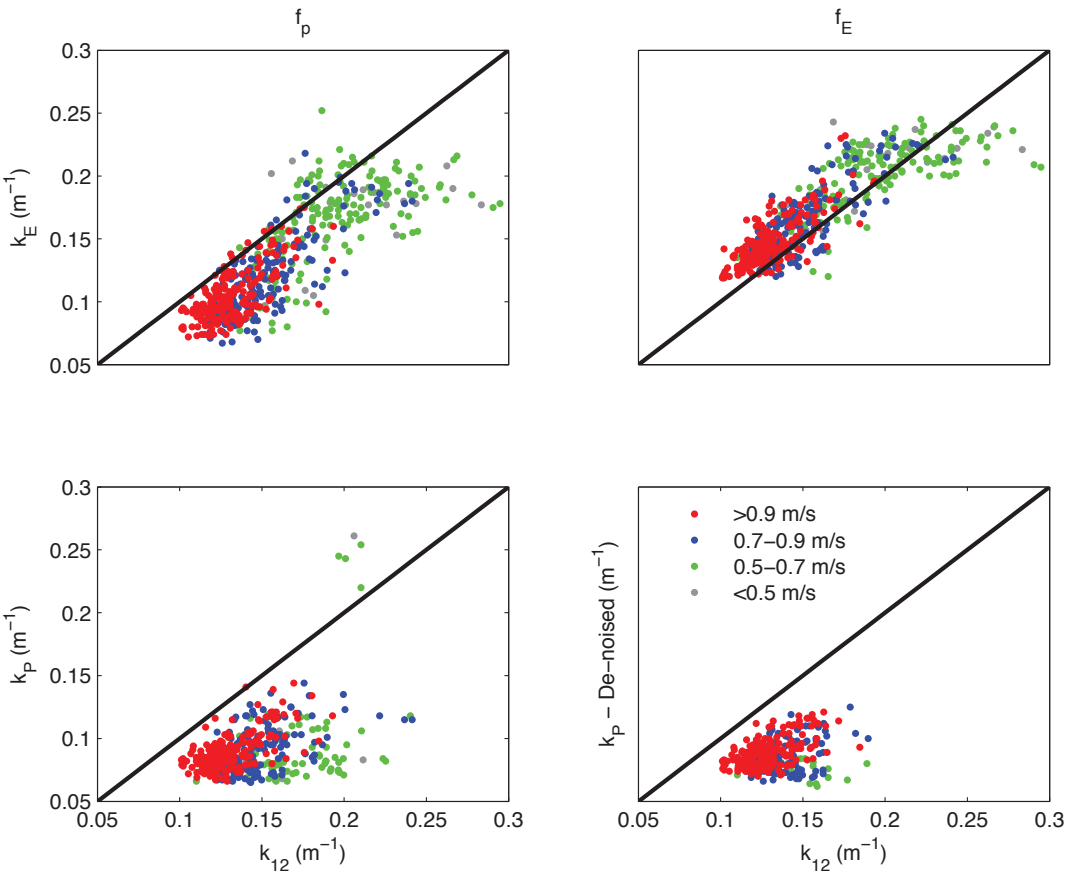

Figure 5.17: Comparing wavenumber estimates from the decay of vertical velocity variance with those from *Kirby and Chen* (1989) for both velocity (k_E) and pressure (k_P) measurements, for peak and energy weighted frequencies on the flood tide. The de-noised means that the noise threshold (the average of pressures outside of the wave-band) was removed.

Figure 5.18 shows the significant wave height estimates, from the decay of velocity variance, velocity spectra with *Kirby and Chen*'s $\tilde{V}$ equation and the pressure. Due to noise, the pressure sensor was not able to resolve waves during non-storm times, so only storm times are displayed. Comparisons of H_s from the decay of velocity variance and from the bottom pressure variance on flood and ebb during storm times are also shown.

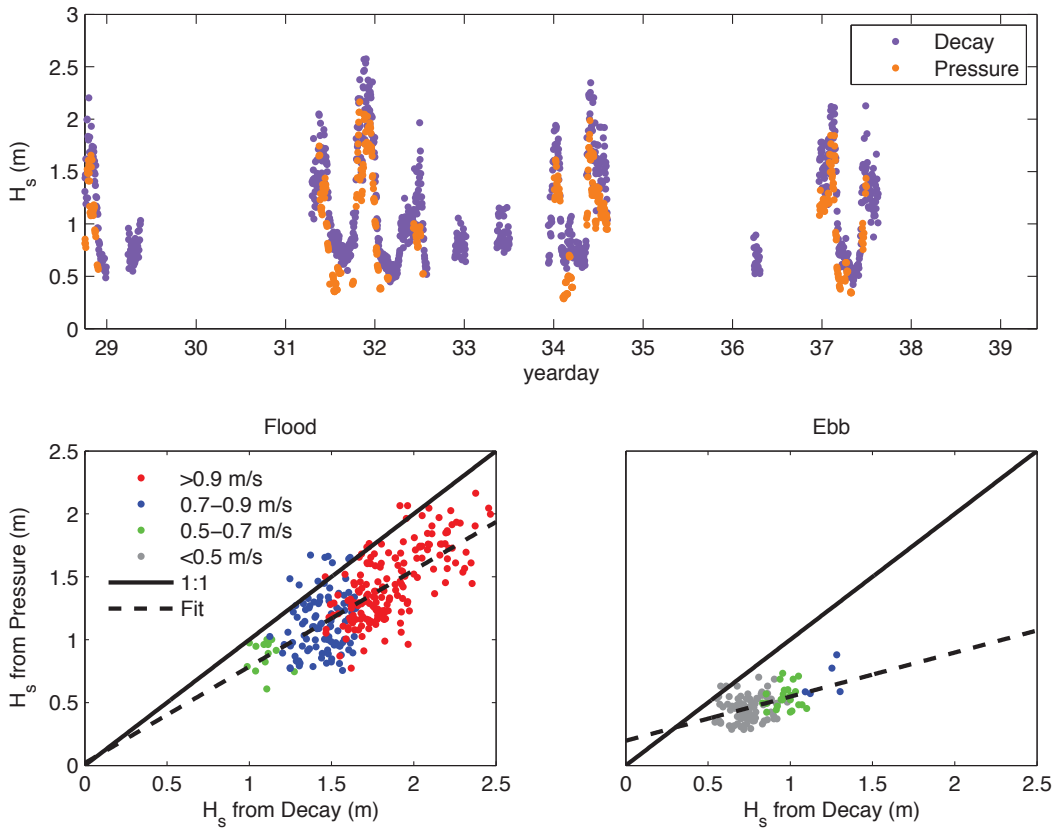

Figure 5.18: Comparing significant wave height estimates from the decay of vertical velocity variance with those using the wavenumber calculated from *Kirby and Chen* (1989) for both velocity and pressure measurements.

Significant wave height estimates obtained from the pressure data are lower than those from the velocity variance decay. The slope of the least-squares linear fit between the values H_s from decay and pressure in Figure 5.18 during flood was 0.77. For comparison, the ratio of the square root of the areas under the spectral peak of Figure 5.14 is 0.89, demonstrating that the lower wave height estimates can be attributed to attenuation of the higher frequency waves. Equation 2.10 was used, which only approximately accounts for the attenuation of pressure with depth. Additionally, the under-prediction of H_s is worse for ebb tide, which coincides with broad-banded wave spectra. From this it can be concluded that (a) Eqn. 2.10 was not sufficient to account for the attenuation, and (b) the error in Eqn. 2.10 was worse for broad-banded waves that tended to occur on ebb.

5.6 Dissipation Rates

The dissipation rate was calculated from the integral of *Kolmogorov* (1941b)'s $f^{-5/3}$ inertial subrange spectrum, and the turbulent noise estimates from Equation 4.9 using $\sigma_D^2 = 0.0045$ m^2/s^2 from Appendix D, yielding the relationship

$$\epsilon = \left[\frac{\sigma_t^2}{C(2\pi/V)^{-2/3}(3/2)[f_1^{-2/3} - f_2^{-2/3}]} \right]^{3/2} \tag{5.5}$$

where C = 2/3 is the second Kolmogorov constant, V is the mid-depth tidal current speed, and f_1 and f_2 represent the upper and lower limits of integration, 1/20 to 1/3 Hz.

5.6.1 Turbulent Noise Time Series

The estimates of σ_t^2 obtained from the variance decay fits are presented in Fig 5.19. The values are tidally modulated, and typically higher during flood than ebb, both during and between storms. Similar ebb/flood asymmetry in the dissipation rate in non-wavy conditions in Grand Passage has been reported by *McMillan et al*. (2016). The purple and green horizontal reference lines in Figure 5.19 indicate the noise levels corresponding to the range of dissipation rates reported by *McMillan et al*. for a 2 m/s flow: 10^{-4} W/kg on flood tide, and 10^{-5} W/kg on ebb.

During non-storm conditions, the present estimates generally lie between the *McMillan et al*. values, which indicates that the present noise estimates even in the absence of waves are representative of actual turbulence levels. Like the *McMillan et al*. results, the highest values occur during flood. The fact that the present peak values during flood are larger than the maximum average values reported by *McMillan et al*. can be attributed to their measurement locations being north of the present position, as it is known that even the sense of this ebb/flood asymmetry varies with location in the channel (*McMillan and Hay*, 2017).

During storm conditions, the values of σ_t^2 during flood tide are much higher, whereas those during ebb are only moderately so. The solid line represents a value of ϵ three times greater than the highest value expected based on the *McMillan et al*. results. The question

is whether these higher values during amplified wave conditions on flood tide are real, or not.

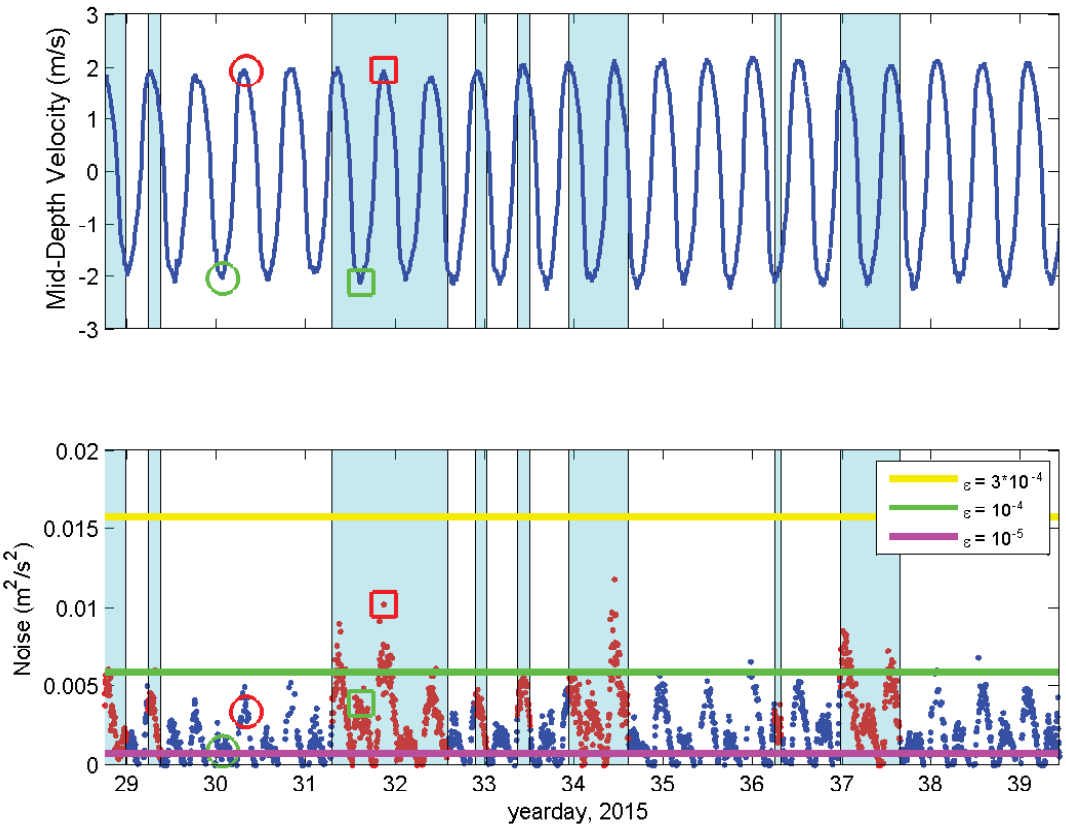

Figure 5.19: Noise time series with Doppler noise removed. Reference lines are the turbulent noise corresponding to the dissipation rates indicated in the legend, calculated with Equation 5.5. The circles are the times selected for the spectra and backscatter figures for non-storm times, and the squares are for storm times.

5.6.2 Velocity Spectra

The top panel of Figure 5.19 shows a time series of mid-depth velocity highlighting the times selected for comparing backscatter to vertical velocity and computing velocity spectra. Spectra of the vertical velocity at 5 and 12 m heights above the bottom, and 85% of the distance to the surface are shown in Figure 5.20 for 5-minute intervals during a peak flood tide and ebb during storm times. Spectral densities were calculated for each beam pair, and combined accounting for pitch and roll. Spectra was calculated with 19 segments, 50% overlap and spectral resolution of 0.0333 Hz, and plotted as loglog with

Doppler noise, from Appendix D ($\sigma_D^2 = 0.0045$ m^2/s^2) removed for comparison to the $f^{-5/3}$ line from *Kolmogorov* (1941a,b), and the work of *Lumley and Terray* (1983).

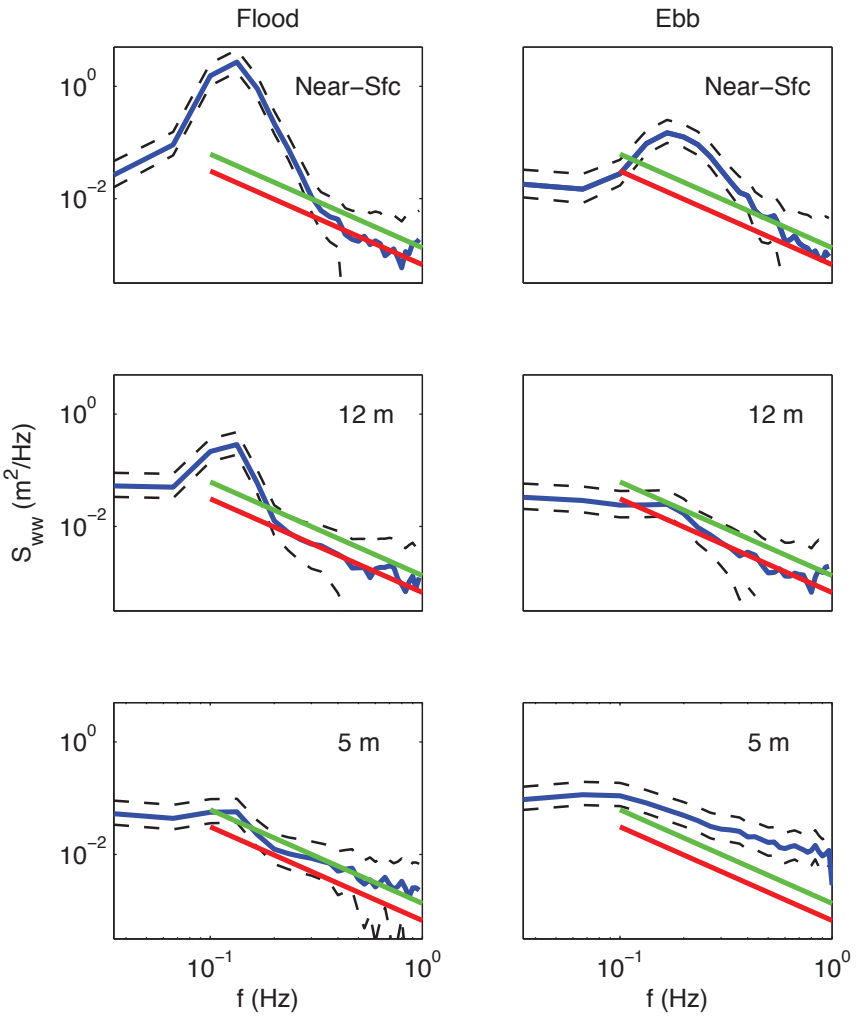

Figure 5.20: 5-minute vertical velocity spectra during storm conditions at the height above bottom indicated in each panel. The blue line is the mean spectral density, and the dashed lines represent the 95% confidence intervals. The red $f^{-5/3}$ reference line is scaled by $\frac{2\pi}{|V|} C\epsilon^{2/3} \frac{2\pi}{|V|}^{-5/3}$ from Eq. 13 of *McMillan and Hay* (2017), with $\epsilon = 10^{-4}$ W/kg. The green reference line is the twice the red. Missing data is due to the subtraction of the Doppler noise.

The agreement between the spectra of vertical velocity and the $f^{-5/3}$ reference line indicates the presence of turbulence, particularly at the near-bottom in wavy conditions. The peak in the spectra between 0.1 and 0.2 Hz on the flood tide indicates the presence of wind wave motion. As expected, the spectral content of the wave energy at mid-depth (12 m)

is shifted to lower frequencies compared to that close to the surface, which implies that estimates of turbulence based on the decay of energy across the wave band are likely to be contaminated by wave energy, and is explored further in Section 5.6.3. The near-bed turbulence levels are much greater on ebb than flood, consistent with the higher shear above the bottom on ebb than flood (see Figure 5.1).

Non-storm conditions were also examined, comparing spectra with the $f^{-5/3}$ line in Figure 5.21.

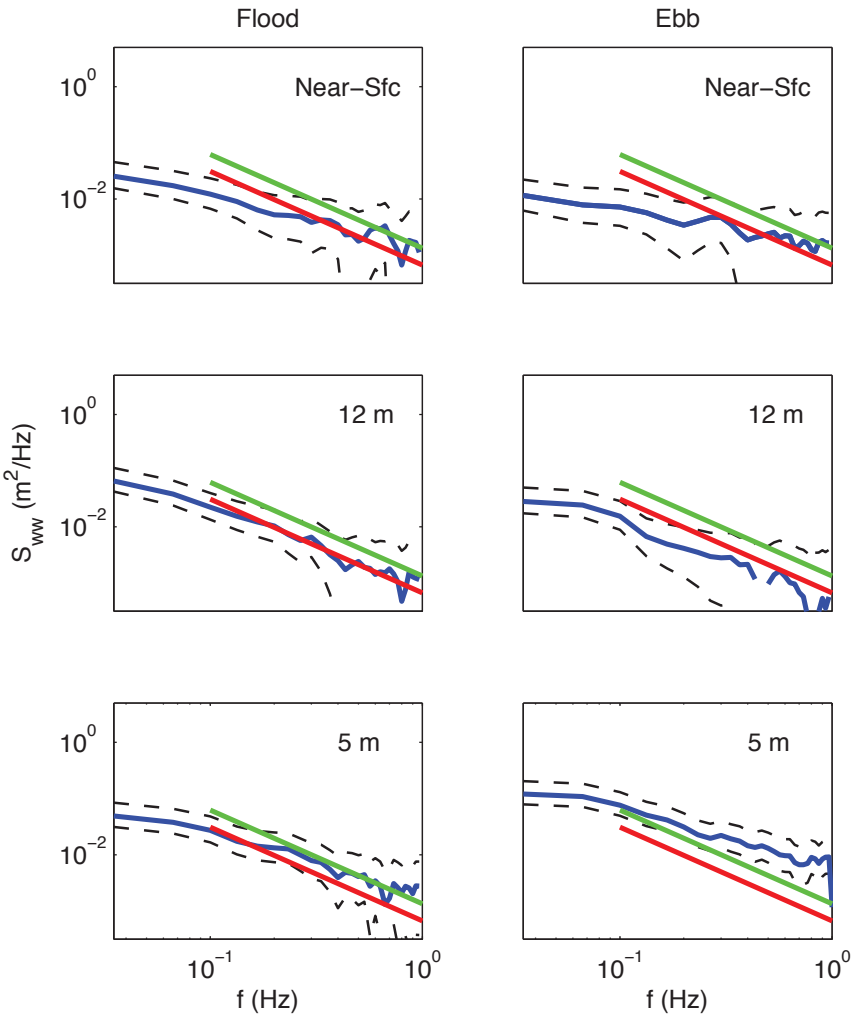

Figure 5.21: 5-minute vertical velocity spectra during non-storm conditions. Lines are as in Figure 5.20.

During the ebb, turbulence levels nearer the bed are again much greater than during flood. During the flood, the spectral densities decrease with approach to the surface, unlike

the storm case. There is no spectral peak in the wave band on either flood or ebb. The higher spectral densities near the bottom, especially on the ebb are a result of aliasing, as determined by *McMillan et al*. (2016).

5.6.3 Dissipation Rates Based on the Peak Wave Frequency

The presence of a peak in the wave-band indicated by the spectra during storm times (Fig 5.20) indicates that wave energy might not be correctly removed from fits to profiles of σ_w^2 based on the variance across the wave band. Consequently, fits were made to the decay with depth of the w spectral density at the spectral peak. The k estimates from the previous waveband variance fits to those from the spectral peak fit are compared in Figure 5.22.

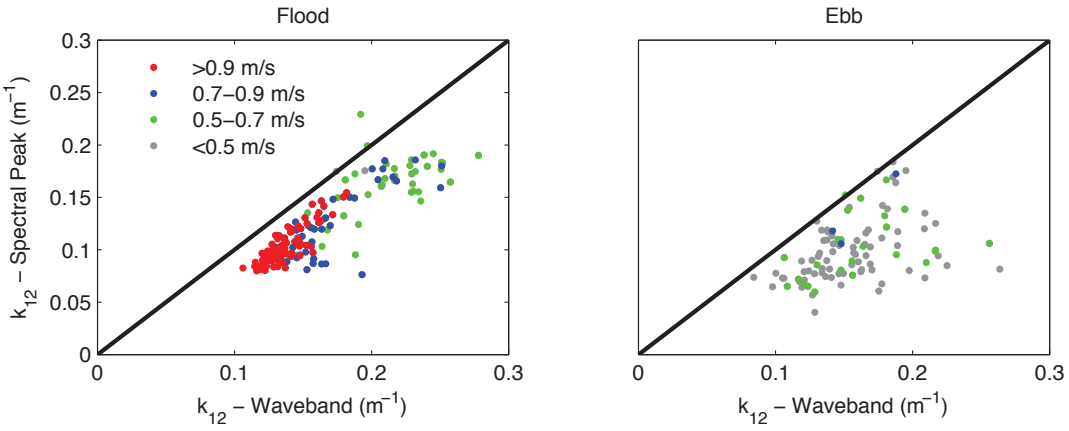

Figure 5.22: Comparing estimates of k from the decay of waveband vertical velocity variance vs the decay of variance at the spectral peak. Legend values are $2\sigma_w$

New estimates of the noise levels were obtained from the fit of the decay of w spectral density at the spectral peak, are shown in Figure 5.23.

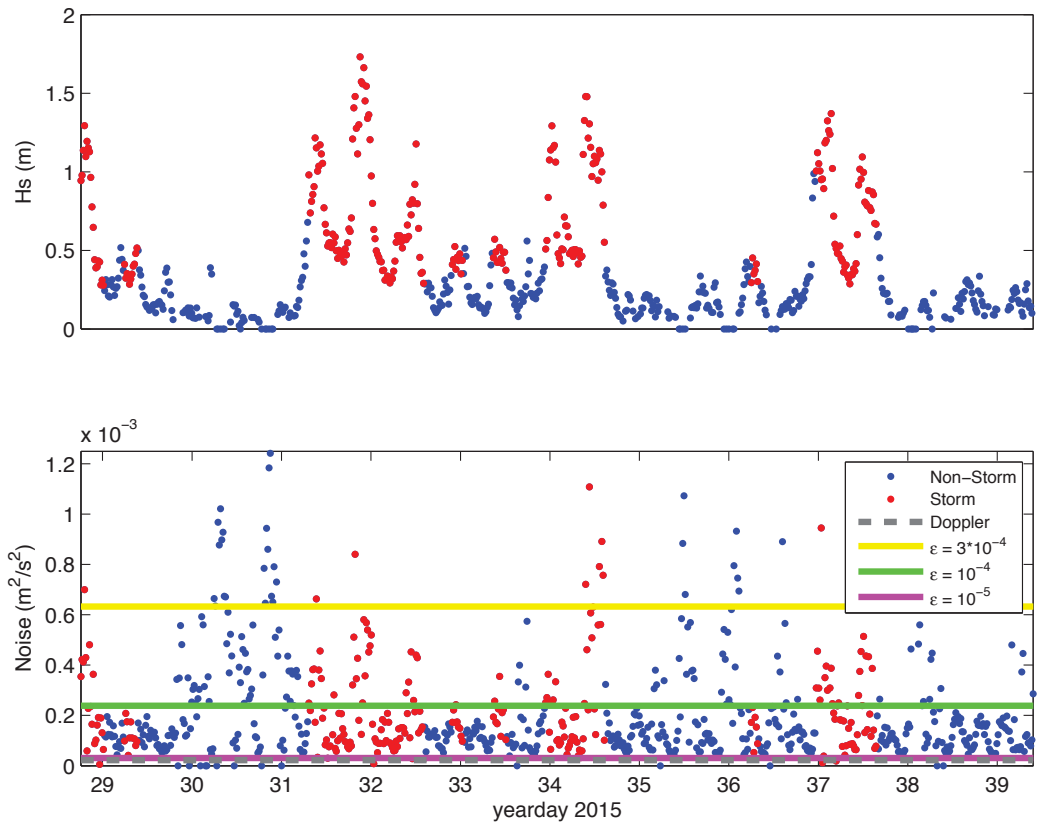

Figure 5.23: H_s from waveband variance and noise estimates from decay of vertical velocity variance at the spectral peak.

The noise levels during storm times are plotted as a function of H_s in Figure 5.24. This shows that on flood tide in particular, noise levels increase with increased wave height.

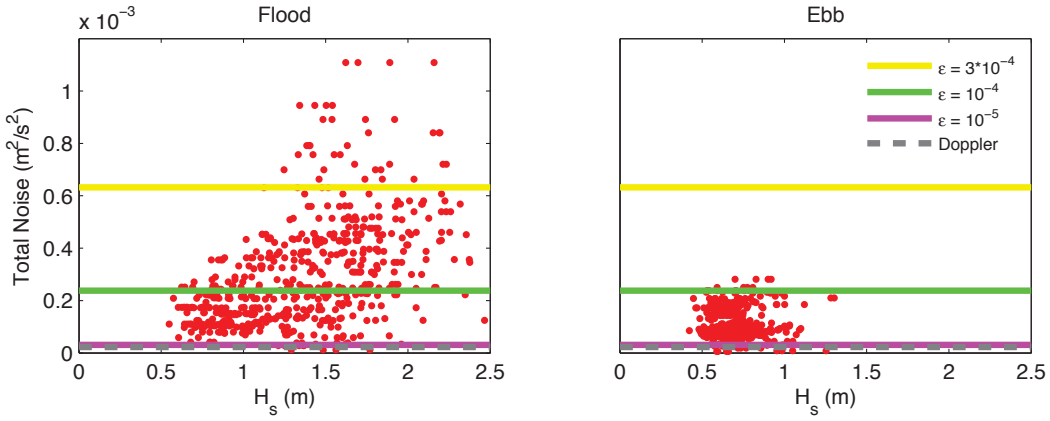

Figure 5.24: H_s from waveband variance and noise estimates from decay of vertical velocity variance at the spectral peak.

5.6.4 Backscatter Amplitude

Higher turbulence levels in the presence of waves might be due to surface-injected turbulence associated with breaking waves. If this were the case, it should be reflected in the ADCP backscatter amplitudes since bubbles are strong scatterers of sound. Figure 5.25 shows the same 5-minute records as Figures 5.20 and 5.21 of backscatter versus time and depth during storm and non-storm times at both peak flood and peak ebb. The higher level of surface-intensified backscatter during the storm compared to non-storm conditions is pronounced. Note as well the higher backscatter levels near the bed during ebb compared to flood, which agrees with the flood/ebb asymmetry seen in the spectra. These higher levels are likely due to increased sediment resuspension during ebb compared to flood, consistent with the previously- mentioned higher turbulence levels and shear near the bottom on ebb compared to flood.

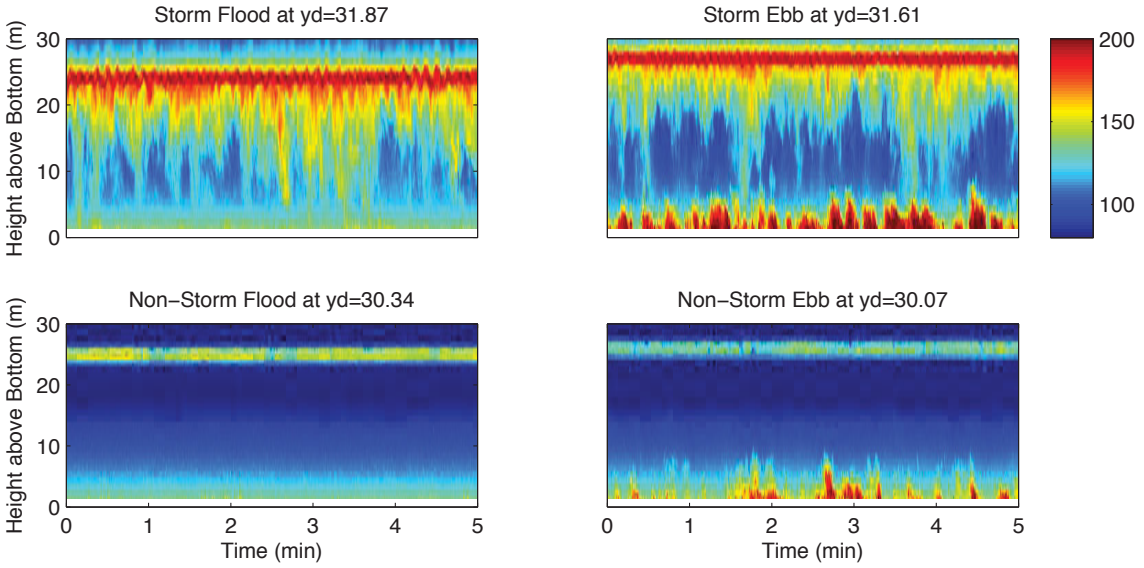

Figure 5.25: Acoustic backscatter on a flood and ebb tide during storm conditions at peak flow, for the same 5-minute segments as the spectra of Figures 5.20 and 5.21 .

To correct the backscatter data for attenuation and spreading losses, the raw backscatter values registered by the ADCP were first converted from “counts” to dB, following *Deines* (1999), and then the range-dependent corrections applied in log space: i.e.,

$$\text{Corrected Backscatter} = \text{(ADCP Backscatter)} 0.45 + 20\log_{10}(r) + 20\log_{10}(e) 2\alpha r \quad (5.6)$$

where r is the radial distance from the transducer and α is the linear attenuation coefficient, 0.0177 m^{-1} (*Francois and Garrison*, 1982). The backscatter corrected for spreading attenuation is shown in Figure 5.26.

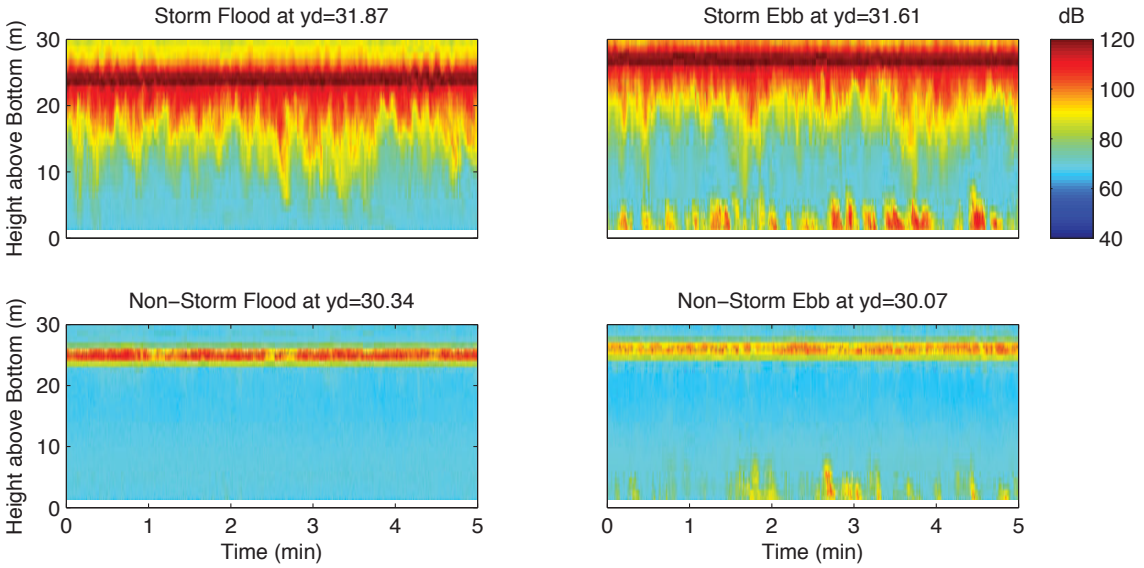

Figure 5.26: Acoustic backscatter on a flood and ebb tide during storm conditions at peak flow, accounting for attenuation and spreading.

The higher acoustic backscatter during storm times points to downward mixing of bubbles from breaking waves, and thus to additional turbulence at depth. The occurrences appear to be more pronounced and frequent on the flood.

CHAPTER 6

CONCLUSION

This thesis examines the wave-current-turbulence interactions in Grand Passage, NS. The objectives were to: (1) determine if the wave number and frequency estimates from a bottom-mounted ADCP in high flow conditions are consistent with the predictions of linear wave theory; (2) determine the values, during storm conditions, of wave statistics as a function of the relative direction of waves and currents during full ebb and full flood; (3) determine if the turbulence dissipation rates are – detectably – influenced by the presence of waves. The work in this thesis resulted in the following conclusions:

- Wavenumber estimates are consistent with linear theory
- Accounting for vertical shear is important
- Higher waves are associated with higher turbulence dissipation rates
- Using beam velocities over the full range of depths is valuable
- Wave heights in Grand Passage are tidally modulated during storm times, and agree with shoaling theory

To overcome the limitations of commercially-available software for extracting wave statistics from ADCP data, a methodology was developed to make use of the data in of all of the range cells in the upper water column. A key feature of this new approach is that it yields an estimate of the turbulence dissipation rate.

The data for the thesis were acquired with a 4-beam 600 kHz bottom-mounted ADCP cabled to shore, oriented such that one of the two orthogonal beam pairs was essentially in line with the mean flow and the incident wave direction. The period of interest was 10 days in late January and early February of 2015, and was characterized by several storm events accompanied by high speed northerly winds.

Profiles of 5-minute averaged along-channel velocity were examined for evidence of changes in mean velocity shear when waves and current are aligned or opposed, the Kemp-Simons effect (*Kemp and Simons*, 1982, 1983; *Groeneweg and Klopman*, 1998), in the Grand Passage data. The ebb/flood asymmetry in the sign of the observed vertical shear in the upper water column is consistent with the Kemp-Simons effect. However, the magnitude of the shear does not change systemically with wave height, contrary to the Kemp-Simons observations.. It is concluded, therefore, that differences in vertical shear of the mean flow between flood and ebb in Grand Passage are due to other dynamical effects. The Kemp-Simons effect is not disproven, but is not observed in these data.

The vertical velocity variance with depth was used to estimate wavenumber by fitting the vertical profile of σ_w^2, the vertical velocity variance in the wave band, to the profile predicted by linear wave theory. The fit was demonstrated to improve with the inclusion of a depth-independent noise term. The agreement between the wavenumber estimates from this fit and the values predicted from the dispersion relation improved with the use of the energy-weighted mean frequency. Including the effect of the Doppler shift improved the agreement on the flood, but not on the ebb. The reasons for this poorer agreement for the ebb tide are unclear, and were not pursued because focus of this thesis was on high wave conditions.

A second wavenumber estimate was obtained from the maximum in the lagged cross-correlation function computed from the along-channel beam velocities. These estimates are in close agreement with those from velocity variance decay, especially with energy-weighted frequency. A third estimate of wavenumber used *Kirby and Chen* (1989)'s theory, accounting for the effect of vertical shear on the Doppler shift. These estimates also agree with those from variance decay, and improved when the energy-weighted frequency was used. The agreement among the three independent wavenumber estimates support the use of the estimates from the vertical velocity variance decay to calculate the wave-current conditions during winter storms in Grand Passage.

Significant wave heights were estimated from the fits to vertical velocity variance extrapolated to the surface, and the associated wavenumber estimates. The wave heights were tidally modulated, and attained maximum values of approximately 2-2.5 m on the flood during peak storm conditions which agrees with shoaling theory of *Dean and Dalrymple* (1991).

Independent estimates of wave height were obtained from the ADCP pressure sensor data. While the wavenumber and water depths correspond to $2.5 < kh < 5$, i.e. nearly deep water waves, the pressure signal from the waves was detectable at the bottom during storms. After correcting for the high noise level in the pressure data, and evaluating the wave energy at spectral peak in the wave band at each depth bin, the estimates of H_s from the pressure data were comparable to, but were consistently about 25% lower than, those from velocity variance decay.

The fits to $\sigma_w^2(z)$ yield, after accounting for Doppler noise, a depth-independent estimate of the vertical component of the turbulent velocity variance in the surface gravity wave band, σ'^2. The σ'^2 values are tidally modulated, increase during storm times, and are higher during flood than ebb both during and between storms. The values of σ'^2 generally fall within the same range as the equivalent turbulent velocity variances computed from the turbulent dissipation rate measurements made by *McMillan et al*. (2016). However, the vertical velocity spectra indicate the expected shift of wave energy to lower frequencies as depth increases. This shift in turn indicates that the residuals from fits to vertical profiles of wave-band-wide wave variance very likely retain some wave energy. Consequently, fits were also made to the vertical profiles of w spectral density at the frequency of the peak of the near-surface w spectrum. The new estimates of σ'^2 were slightly reduced from those from the waveband decay fit. On average, these σ'^2 estimates tend to increase with increasing wave height during flood tide.

Pursuant to the observed association between σ'^2 and H_s during flood, the backscatter amplitude was also examined for evidence of breaking waves, since wave breaking accompanied by the vigorous stirring associated with the background tidal turbulence represents a potential source of additional turbulence at depth. During storm times, downward mixing of bubbles from breaking waves is indicated by the backscatter data, and qualitatively indicates bubble penetration to greater depths on flood than ebb. During non-storm times, for which waves are either absent or have very low amplitudes, these bubble plumes are not present.

The results of this thesis are important on a basic scientific level, contributing both to an improved understanding of wave-current-turbulence interactions, and to the use of acoustic Doppler systems for remote measurements of wave statistics and turbulence in

high flow, high wave conditions. This research has applied significance for the implementation of in-stream tidal turbines, via improved knowledge of flow variability in high flow tidal channels.

APPENDIX A

BEAM 1 AND 2 ROLL CORRECTION

Figure A.1 illustrates the ADCP in its deployed state viewed from the side and from above. In the side view, the schematic demonstrates how errors produced by *WavesMon* can occur, with one beam measuring at a crest and the other at a trough. The error induced by not accounting for pitch and roll is also illustrated: i.e a change in the beam angle results in a change in the depth of bin measurement.

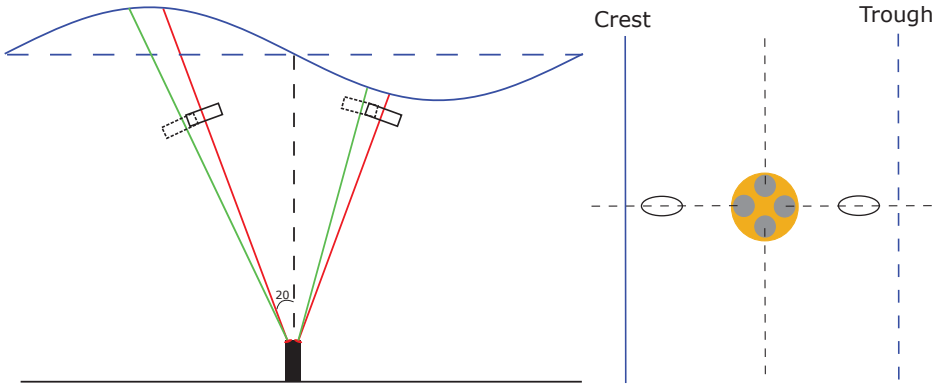

Figure A.1: (a) Along-channel side view of the ADCP. The red lines indicate the beams inclined at 20^0, and the green indicate the impact of pitch/roll, with the boxes representing range cells. (b) Top view of the ADCP, with ovals representing surface bins along-channel.

Figure A.2 demonstrates the effect that accounting for the roll has on the beam velocity variance measurements.

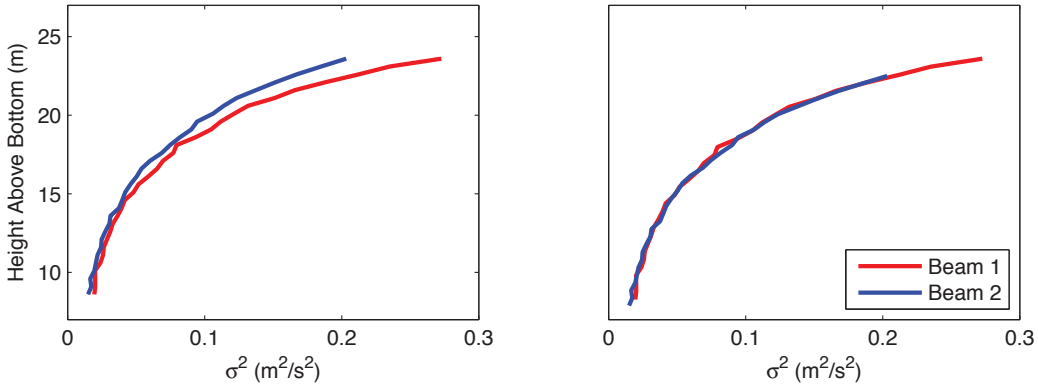

Figure A.2: The left hand panel shows the decay of beam velocity variance with depth, if the beam angle was assumed to be 20^0. The right hand panel shows the same beam velocity variances, but at the correct depths when the roll is accounted for.

APPENDIX B

2-BEAM CORRELATION FUNCTION

For deep water waves, following Figure B.1 with the conventions of with beam 4 to the left, beam 3 to the right and waves propagating to the left, a lagged 2-beam cross-correlation function was developed to obtain an estimate of wavenumber.

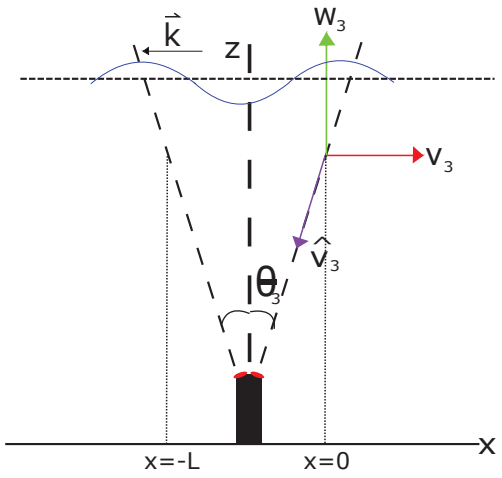

Figure B.1: The across-channel convention for velocity measurement where θ_3 is the angle of beam 3 with respect to the vertical, $\hat{v}_3$ is the beam velocity, v and w are the horizontal along-channel and vertical velocities respectively and L is the beam separation.

For a sinusoidal wave propagating in the negative along-channel direction (i.e. corresponding to waves from the north)

$$v = \cos(ky + \omega_0 t) \tag{B.1}$$

and

$$w = \sin(ky + \omega_0 t) \tag{B.2}$$

where k is the local wavenumber and ω_0 is the observed wave frequency.

For beam 3 (downstream on flood, as Figure 3.3) at $y = 0$

$$v_3 = \cos \omega_0 t \tag{B.3a}$$

$$w_3 = \sin \omega_0 t \tag{B.3b}$$

and beam 4 upstream at $y = -L$

$$v_4 = \cos(\omega_0 t - kL) \tag{B.4a}$$

$$w_4 = \sin(\omega_0 t - kL) \tag{B.4b}$$

The corresponding beam velocities are

$$\hat{v}_3 = -\sin \theta_3 v_3 - \cos \theta_3 w_3 \tag{B.5a}$$

$$\hat{v}_4 = \sin \theta_4 v_4 - \cos \theta_4 w_4 \tag{B.5b}$$

so,

$$\hat{v}_3(t) = -\sin \theta_3 \cos \omega_0 t - \cos \theta_3 \sin \omega_0 t \tag{B.6a}$$

$$\hat{v}_4(t + \tau) = \sin \theta_4 \cos(\omega_0 t + \phi) - \cos \theta_4 \sin(\omega_0 t + \phi) \tag{B.6b}$$

where $\phi = \omega_0 \tau - kL$ and τ is the time lag between beams 3 and 4 at separation L.

Rearranging Eq. B.6b,

$$\hat{v}_4(t + \tau) = \cos \omega_0 t(\sin \theta_4 \cos \phi - \cos \theta_4 \sin \phi) - \sin \omega_0 t(\sin \theta_4 \sin \phi + \cos \theta_4 \cos \phi) \tag{B.7}$$

The variance at the lag τ is

$$R_{34}(\tau) = -\frac{1}{2}\sin\theta_3(\sin\theta_4\cos\phi - \cos\theta_4\sin\phi) + \frac{\cos\theta_4}{2}(\sin\theta_4\sin\phi + \cos\theta_4\cos\phi) \quad \text{(B.8)}$$

which has a maximum value at

$$\tan\phi = \frac{\tan\theta_3 + \tan\theta_4}{1 - \tan\theta_3\tan\theta_4} \quad \text{(B.9)}$$

For $\theta_3 = \theta_4 = \theta$, Equation B.9 reduces to

$$\tan\phi = \tan 2\theta \quad \text{(B.10)}$$

and so

$$kL = \omega_0\tau - 2\theta \quad \text{(B.11)}$$

For the pitch of the ADCP (-1.93^o) during the selected storm, Equation B.9 and B.10 yield the same value for $\tan\phi$.

For finite water depth, it can be shown that the equivalent expression is

$$\tan\phi = \frac{\tanh kh\sin 2\theta}{\tanh^2 kh\cos^2\theta - \sin^2\theta} \quad \text{(B.12)}$$

where h is the mean water depth.

APPENDIX C

WAVE HEIGHT FROM EMPIRICAL ESTIMATES

As outlined in *Kamphuis* (2000), estimates of wind wave properties – e.g. height and period – can be made with the empirical Jonswap parameters,

$$F^* = \frac{gF}{U^2}, H^*_{mo} = \frac{gH_{mo}}{U^2}, T^*_p = \frac{gT_p}{U}, t^* = \frac{gt}{U} \tag{C.1}$$

and the relationships

$$H^*_{mo} = 0.0016(F^*)^{1/2}, T^*_p = 0.286(F^*)^{1/3}, t^* = 68.8(F^*)^{2/3} \tag{C.2}$$

where F is fetch length, H_{mo} is the significant wave height, t is the wind duration, T_p is the peak wave period, and U is the wind speed. The starred variables are the dimensionless counterparts of these parameters. The effective fetch, F_{eff}, is the fetch for unlimited duration.

$$F^*_{eff} = \left(\frac{t^*}{68.8}\right)^{1/2} \tag{C.3}$$

If $F^* \ll F^*_{eff}$, the waves are fetch-limited and the value of F^* is used in calculation of the Jonswap relationships. If not, F^*_{eff} is used.

For Grand Passage during the storm conditions with wind from the north, the fetch is approximately 100 km. Wind speeds exceeded 60 km/h for 12 hours during the January 31 storm. Using these values, the waves are found to be fetch limited, and thus the F^* value was used. The Jonswap relationship and parameter equations yielded estimates of

H_{mo} = 2.7 m and T_p = 7.4 s. This agrees with the manual wave forecasting diagram by *Groen and Dorrestein* (1976).

The empirical estimates are based on the assumption of steady wind from a constant direction and no mean current. Therefore, the estimates should be compared with ADCP wave height estimates during slack tide, which reach maximum storm values of about 1.5 m. If the empirical estimates are accurate, they suggest that the wave energy losses due to refraction before the measurement location reduces wave heights by approximately half. However, the WCI on the flooding tide approximately compensates for this loss.

APPENDIX D

DOPPLER NOISE

D.1 Single Ping Error in u

$$\hat{v}_1 = u_1 \sin\theta - w_1 \cos\theta + n_1 \tag{D.1}$$

$$\hat{v}_2 = -u_2 \sin\theta - w_2 \cos\theta + n_2 \tag{D.2}$$

Assuming $u_1 = u_2$ and $w_1 = w_2$, combining Equations D.1 and D.2 gives

$$\hat{v}_1 - \hat{v}_2 = 2u \sin\theta + n_1 - n_2 \tag{D.3}$$

So

$$u = \frac{\hat{v}_1 - \hat{v}_2}{2\sin\theta} - \frac{n_1 - n_2}{2\sin\theta} \tag{D.4}$$

$$u^2 = \frac{(\hat{v}_1 - \hat{v}_2)^2}{4\sin^2\theta} - \frac{n_1^2 - n_2^2}{4\sin^2\theta} \tag{D.5}$$

so the mean square error (MSE) of u is

$$\text{MSE}_u = \frac{\sigma_n^2}{2\sin^2\theta} \tag{D.6}$$

and the root mean square (RMS) error of u, δ_u is

$$\delta_u = \frac{\sigma_n}{\sqrt{2}\sin\theta} \tag{D.7}$$

For the ADCP settings here, the value of δ_u, based on the manufacturer's instrument set-up software, is 13 cm/s

D.2 Single Ping Error in σ_w

From Equations D.1 and D.2,

$$\sigma_1^2 = \sigma_{u1}^2 \sin^2\theta + \sigma_{w1}^2 \cos^2\theta - 2\overline{u_1 w_1}\sin\theta\cos\theta + \sigma_{n1}^2 \tag{D.8}$$

$$\sigma_2^2 = \sigma_{u2}^2 \sin^2\theta + \sigma_{w2}^2 \cos^2\theta - 2\overline{u_2 w_2}\sin\theta\cos\theta + \sigma_{n2}^2 \tag{D.9}$$

since $\sigma_{u1}^2 = \sigma_{u2}^2 = \sigma_u^2$, $\overline{u_1 w_1} = \overline{u_2 w_2}$ and $\sigma_{n1}^2 = \sigma_{n2}^2 = \sigma_n^2$

$$\sigma_1^2 + \sigma_2^2 = 2\sigma_u^2 \sin^2\theta + 2\sigma_w^2 \cos^2\theta + 2\sigma_n^2 \tag{D.10}$$

$$\sigma_w^2 + \sigma_u^2 \tan^2\theta = \frac{\sigma_1^2 + \sigma_2^2}{2\cos^2\theta} - \frac{\sigma_n^2}{\cos^2\theta} \tag{D.11}$$

Thus if $\sigma_u^2 = 0$, contribution of the Doppler noise to σ_w^2, σ_D^2 is,

$$\sigma_D^2 = \frac{\sigma_n^2}{\cos^2\theta} = \frac{2\sin^2\theta\delta_u^2}{\cos^2\theta} = 2\tan^2\theta\delta_u^2 \tag{D.12}$$

With δ_u = 0.13 m/s, σ_D^2 = 0.0045 m^2/s^2.

BIBLIOGRAPHY

Ahmadian, R., and R. A. Falconer, Assessment of array shape of tidal stream turbines on hydro-environmental impacts and power output, *Renewable Energy*, *44*, 318–327, 2012.

Ardhuin, F., A. Roland, F. Dumas, A.-C. Bennis, A. Sentchev, P. Forget, J. Wolf, F. Girard, P. Osuna, and M. Benoit, Numerical wave modeling in conditions with strong currents: Dissipation, refraction, and relative wind, *Journal of Physical Oceanography*, *42*, 2101–2120, 2012.

Ashall, L. M., R. P. Mulligan, and B. A. Law, Variability in suspended sediment concentration in the Minas Basin, Bay of Fundy, and implications for changes due to tidal power extraction, *Coastal Engineering*, *107*, 102–115, 2016.

Atwater, J. F., and G. A. Lawrence, Regulatory, design and methodological impacts in determining tidal-in-stream power resource potential, *Energy Policy*, *39*, 1694–1698, 2011.

Bahaj, A., A. Molland, J. Chaplin, and W. Batten, Power and thrust measurements of marine current turbines under various hydrodynamic flow conditions in a cavitation tunnel and a towing tank, *Renewable Energy*, *32*, 407–426, 2007.

Blunden, L., and A. Bahaj, Initial evaluation of tidal stream energy resources at Portland Bill, UK, *Renewable Energy*, *31*, 121–132, 2006.

Booij, N., L. Holthuijsen, and R. Ris, The "SWAN" wave model for shallow water, in *Coastal Engineering 1996*, pp. 668–676, 1997.

Brooks, D. A., The tidal-stream energy resource in Passamaquoddy–Cobscook Bays: a fresh look at an old story, *Renewable Energy*, *31*, 2284–2295, 2006.

Cummins, P. F., On the extractable power from a tidal channel, *Journal of Waterway, Port, Coastal, and Ocean Engineering*, *138*, 63–71, 2011.

Cummins, P. F., The extractable power from a split tidal channel: An equivalent circuit analysis, *Renewable Energy*, *50*, 395–401, 2013.

Dean, R. G., and R. A. Dalrymple, *Water Wave Mechanics for Engineers and Scientists*, vol. 2, World Scientific Publishing Co Inc, 1991.

Deines, K. L., Backscatter estimation using broadband acoustic Doppler current profilers, in *Current Measurement, 1999. Proceedings of the IEEE sixth working conference on*, pp. 249–253, IEEE, 1999.

Dodet, G., X. Bertin, N. Bruneau, A. B. Fortunato, A. Nahon, and A. Roland, Wave-current interactions in a wave-dominated tidal inlet, *Journal of Geophysical Research: Oceans*, *118*, 1587–1605, 2013.

Fisch, J. G., Tidal energy law in Canada: Hindering an untapped potential for international primacy, *Appeal: Rev. Current L. & L. Reform*, *21*, 37, 2016.

Forristall, G. Z., Measurements of a saturated range in ocean wave spectra, *Journal of Geophysical Research: Oceans*, *86*, 8075–8084, 1981.

Francois, R., and G. Garrison, Sound absorption based on ocean measurements: Part I: Pure water and magnesium sulfate contributions, *The Journal of the Acoustical Society of America*, *72*, 896–907, 1982.

Garrett, C., and P. Cummins, The power potential of tidal currents in channels, in *Proceedings of the Royal Society of London A: Mathematical, Physical and Engineering Sciences*, vol. 461, pp. 2563–2572, The Royal Society, 2005.

Grant, W. D., and O. S. Madsen, Combined wave and current interaction with a rough bottom, *Journal of Geophysical Research: Oceans*, *84*, 1797–1808, 1979.

Grant, W. D., and O. S. Madsen, The continental-shelf bottom boundary layer, *Annual Review of Fluid Mechanics*, *18*, 265–305, 1986.

Groen, P., and R. Dorrestein, Zeegolven. KNMI Opstellen op Oceanografisch en Maritiem Meteorologisch Gebied, *Dutch. State Printing Office, The Hague*, 1976.

Groeneweg, J., and G. Klopman, Changes of the mean velocity profiles in the combined wave–current motion described in a GLM formulation, *Journal of Fluid Mechanics*, *370*, 271–296, 1998.

Gunawan, B., V. S. Neary, and J. Colby, Tidal energy site resource assessment in the East River tidal strait, near Roosevelt Island, New York, New York, *Renewable Energy*, *71*, 509–517, 2014.

Hasegawa, D., J. Sheng, D. A. Greenberg, and K. R. Thompson, Far-field effects of tidal energy extraction in the Minas Passage on tidal circulation in the Bay of Fundy and Gulf of Maine using a nested-grid coastal circulation model, *Ocean Dynamics*, *61*, 1845–1868, 2011.

Hashemi, M. R., S. P. Neill, P. E. Robins, A. G. Davies, and M. J. Lewis, Effect of waves on the tidal energy resource at a planned tidal stream array, *Renewable Energy*, *75*, 626–639, 2015.

Hashemi, M. R., S. T. Grilli, and S. P. Neill, A simplified method to estimate tidal current effects on the ocean wave power resource, *Renewable Energy*, *96*, 257–269, 2016.

Hay, A., R. Karsten, G. Trowse, D. Morin, T. Webster, J. McMillan, M. O'Flaherty-Sproul, D. Schillinger, R. Cheel, E. Marshall, et al., Southwest Nova Scotia Resource Assessment, 2013a.

Hay, A. E., J. McMillan, R. Cheel, and D. Schillinger, Turbulence and drag in a high Reynolds number tidal passage targeted for in-stream tidal power, in *Oceans-San Diego, 2013*, pp. 1–10, IEEE, 2013b.

Kamphuis, J. W., *Introduction to Coastal Engineering and Management*, vol. 16, World Scientific Publishing Co Inc, 2000.

Karsten, R., A. Swan, and J. Culina, Assessment of arrays of in-stream tidal turbines in the Bay of Fundy, *Phil. Trans. R. Soc. A*, *371*, 20120189, 2013.

Karsten, R. H., J. McMillan, M. Lickley, and R. Haynes, Assessment of tidal current energy in the Minas Passage, Bay of Fundy, *Proceedings of the Institution of Mechanical Engineers, Part A: Journal of Power and Energy*, *222*, 493–507, 2008.

Kemp, P., and R. Simons, The interaction between waves and a turbulent current: waves propagating with the current, *Journal of Fluid Mechanics*, *116*, 227–250, 1982.

Kemp, P., and R. Simons, The interaction of waves and a turbulent current: waves propagating against the current, *Journal of Fluid Mechanics*, *130*, 73–89, 1983.

Kirby, J. T., and T.-M. Chen, Surface waves on vertically sheared flows: approximate dispersion relations, *Journal of Geophysical Research: Oceans*, *94*, 1013–1027, 1989.

Klopman, G., Vertical structure of the flow due to waves and currents, *Progress report, Delft Hydraulics H*, *840*, 1994.

Kolmogorov, A. N., The local structure of turbulence in incompressible viscous fluid for very large Reynolds numbers, in *Dokl. Akad. Nauk SSSR*, vol. 30, pp. 299–303, 1941a.

Kolmogorov, A. N., Dissipation of energy in locally isotropic turbulence, in *Dokl. Akad. Nauk SSSR*, vol. 32, pp. 16–18, 1941b.

Kundu, P., and I. Cohen, Fluid mechanics, 759 pp, 2004.

Longuet-Higgins, M. S., and R. Stewart, Radiation stresses in water waves; a physical discussion, with applications, in *Deep Sea Research and Oceanographic Abstracts*, vol. 11, pp. 529–562, Elsevier, 1964.

Lumley, J., and E. Terray, Kinematics of turbulence convected by a random wave field, *Journal of Physical Oceanography*, *13*, 2000–2007, 1983.

Malinka, C., A. Hay, and R. Cheel, Toward acoustic monitoring of marine mammals at a tidal turbine site: Grand Passage, NS, Canada, *Proc. of EWTEC*, pp. 1–10, 2015.

McMillan, J. M., and A. E. Hay, Spectral and structure function estimates of turbulence dissipation rates in a high-flow tidal channel using broadband ADCPs, *Journal of Atmospheric and Oceanic Technology*, *34*, 5–20, 2017.

McMillan, J. M., A. E. Hay, R. G. Lueck, and F. Wolk, Rates of dissipation of turbulent kinetic energy in a high Reynolds number tidal channel, *Journal of Atmospheric and Oceanic Technology*, *33*, 817–837, 2016.

Mei, C. C., *The applied dynamics of ocean surface waves*, vol. 1, World Scientific Publishing Co. Pte. Ltd., 1989.

Mei, C. C., M. Stiassnie, and D. K.-P. Yue, *Theory and applications of ocean surface waves: nonlinear aspects*, vol. 23, World scientific, 2005.

Mycek, P., B. Gaurier, G. Germain, G. Pinon, and E. Rivoalen, Experimental study of the turbulence intensity effects on marine current turbines behaviour. Part I: One single turbine, *Renewable Energy*, *66*, 729–746, 2014a.

Mycek, P., B. Gaurier, G. Germain, G. Pinon, and E. Rivoalen, Experimental study of the turbulence intensity effects on marine current turbines behaviour. Part II: Two interacting turbines, *Renewable Energy*, *68*, 876–892, 2014b.

Nielsen, P., *Coastal Bottom Boundary Layers and Sediment Transport*, vol. 4, World Scientific Publishing Co Inc., 1992.

Peregrine, D., Interaction of water waves and currents, *Advances in Applied Mechanics*, *16*, 9–117, 1976.

Polagye, B., M. Kawase, and P. Malte, In-stream tidal energy potential of Puget Sound, Washington, *Proceedings of the Institution of Mechanical Engineers, Part A: Journal of Power and Energy*, *223*, 571–587, 2009.

Richardson, L. F., *Weather Prediction by Numerical Process*, Cambridge University Press, 1922.

Ris, R., and L. Holthuijsen, Spectral modelling of current induced wave-blocking, in *Coastal Engineering 1996*, pp. 1247–1254, 1997.

Rusu, L., M. Bernardino, and C. G. Soares, Modelling the influence of currents on wave propagation at the entrance of the Tagus Estuary, *Ocean Engineering*, *38*, 1174–1183, 2011.

Saruwatari, A., D. M. Ingram, and L. Cradden, Wave–current interaction effects on marine energy converters, *Ocean Engineering*, *73*, 106–118, 2013.

Smith, J. A., Wave–current interactions in finite depth, *Journal of Physical Oceanography*, *36*, 1403–1419, 2006.

Stewart, R. H., and J. W. Joy, HF radio measurements of surface currents, in *Deep Sea Research and Oceanographic Abstracts*, vol. 21, pp. 1039–1049, Elsevier, 1974.

Terray, E., R. L. Gordon, and B. Brumley, Measuring wave height and direction using upward-looking ADCPs, in *OCEANS'97. MTS/IEEE Conference Proceedings*, vol. 1, pp. 287–290, IEEE, 1997.

Terray, E. A., B. H. Brumley, and B. Strong, Measuring waves and currents with an upward-looking ADCP, in *Current Measurement, 1999. Proceedings of the IEEE Sixth Working Conference on*, pp. 66–71, IEEE, 1999.

Thornton, E. B., and R. Guza, Transformation of wave height distribution, *Journal of Geophysical Research: Oceans*, *88*, 5925–5938, 1983.

Townsend, M., and J. D. Fenton, A comparison of analysis methods for wave pressure data, *Coastal Engineering Proceedings*, *1*, 1996.

van der Westhuysen, A. J., Spectral modeling of wave dissipation on negative current gradients, *Coastal Engineering*, *68*, 17–30, 2012.

VanZwieten, J., W. McAnally, J. Ahmad, T. Davis, J. Martin, M. Bevelhimer, A. Cribbs, R. Lippert, T. Hudon, and M. Trudeau, In-stream hydrokinetic power: review and appraisal, *Journal of Energy Engineering*, *141*, 04014024, 2014.

Wargula, A., B. Raubenheimer, and S. Elgar, Wave-driven along-channel subtidal flows in a well-mixed ocean inlet, *Journal of Geophysical Research: Oceans*, *119*, 2987–3001, 2014.

Wolf, J., and D. Prandle, Some observations of wave–current interaction, *Coastal Engineering*, *37*, 471–485, 1999.

Yang, Z., T. Wang, A. Copping, and S. Geerlofs, Modeling of in-stream tidal energy development and its potential effects in Tacoma Narrows, Washington, USA, *Ocean & Coastal Management*, *99*, 52–62, 2014.

Zhou, Z., F. Scuiller, J. F. Charpentier, M. Benbouzid, and T. Tang, An up-to-date review of large marine tidal current turbine technologies, in *Power Electronics and Application Conference and Exposition (PEAC), 2014 International*, pp. 480–484, IEEE, 2014.